

Navigation Using Inertial Sensors

Paul D. Groves
University College London
United Kingdom

This tutorial provides an introduction to navigation using inertial sensors, explaining the underlying principles. Topics covered include accelerometer and gyroscope technology and their characteristics, strapdown inertial navigation, attitude determination, integration and alignment, zero updates, motion constraints, pedestrian dead reckoning using step detection, and fault detection.

I. INTRODUCTION

Inertial sensors comprise accelerometers, which measure specific force, and gyroscopes, commonly abbreviated to gyros, which measure angular rate. An inertial measurement unit (IMU) combines multiple accelerometers and gyros, usually three of each, to produce three-dimensional measurements of specific force and angular rate. By integrating these measurements and applying a gravity model, a position, velocity, and attitude solution may be maintained, a concept known as inertial navigation.

Practical inertial navigation systems (INSs) have been available from the 1950s but were initially large and expensive. In early INSs, the sensors were physically aligned horizontally and vertically by mounting them on a platform connected to the host body by a series of gimbals driven by motors. This was known as a platform configuration and resulted from the limitations of early gyro technology and the need to minimize the computational load. The strapdown configuration, whereby the sensors are aligned with the host body, was first proposed in 1962 [1] with production of the first aircraft systems starting at the end of the 1970s [2]. Today, it is almost universal. Inertial sensors are now available with a range of physical and performance characteristics at costs ranging from a few dollars to hundreds of thousands of dollars.

This tutorial provides an introduction to navigation using inertial sensors, covering a range of topics and explaining the underlying principles. Section II describes how accelerometers and gyros work and introduces the IMU. Section III reviews their error characteristics. Strapdown inertial navigation is ex-

plained in Section IV, including the basic principles, initialization, navigation equations, and error propagation. Section V describes absolute attitude determination using inertial sensors, both alone and with magnetometers. Section VI explains how inertial navigation performance is improved through integration with other sensors. Section VII introduces zero updates and motion constraints. Section VIII introduces pedestrian dead reckoning (PDR) using step detection, an alternative navigation technique. Finally, Section IX discusses fault detection and Section X presents concluding remarks.

The notation, conventions, and terminology are based on [3], which provides further details of most of the topics covered.

II. INERTIAL SENSORS

This section describes the basic principles of the accelerometer and gyro, compares the different types of sensors, and then explains how they are incorporated into an IMU. Inertial sensor technology is described in more detail in [3–5].

A. ACCELEROMETERS

Fig. 1 shows a simple accelerometer. A proof mass is free to move with respect to the accelerometer case along the accelerometer's sensitive axis, restrained by springs. A pickoff measures the position of the mass with respect to the case. When an accelerating force along the sensitive axis is applied to the case, the proof mass initially continues at its previous velocity, so the case moves with respect to the mass, compressing one spring and stretching the other. This alters the forces the springs transmit. Consequently, the case moves with respect to the mass until the acceleration of the mass due to the asymmetric forces exerted by the springs matches the acceleration of the case due to the externally applied force. The resultant position of the mass with respect to the case is proportional to the applied acceleration. By measuring this with a pickoff, an acceleration measurement is obtained.

An important exception is gravitational acceleration. This acts on the proof mass directly, not via the springs, and applies the same acceleration to all components of the accelerometer, so there is no relative motion of the mass with respect to the case. Therefore, accelerometers sense only the nongravitational acceleration, known as specific force. People also sense specific force. The sensation of weight is caused by the forces opposing gravity, known as the restoring force on land, buoyancy at sea, and lift in the air. During freefall, the specific force is zero, so there is no sensation of weight. Conversely, under zero accel-

Author's current address: UCL Engineering, Chadwick Building, University College London, Gower Street, London, WC1E 6BT, United Kingdom E-mail: (p.groves@ucl.ac.uk).

Manuscript received November 10, 2013; revised March 31, 2014; released for publication April 21, 2014.

DOI. No. 10.1109/MAES.2014.130191.

Review handled by P. Willett.

0885/8985/14/ \$26.00 © 2015 IEEE

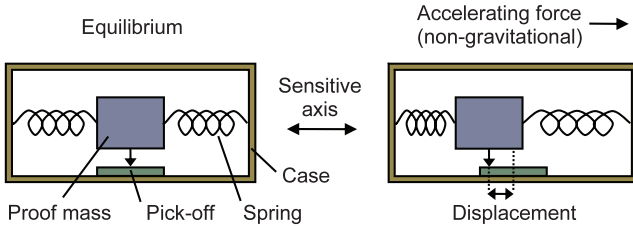
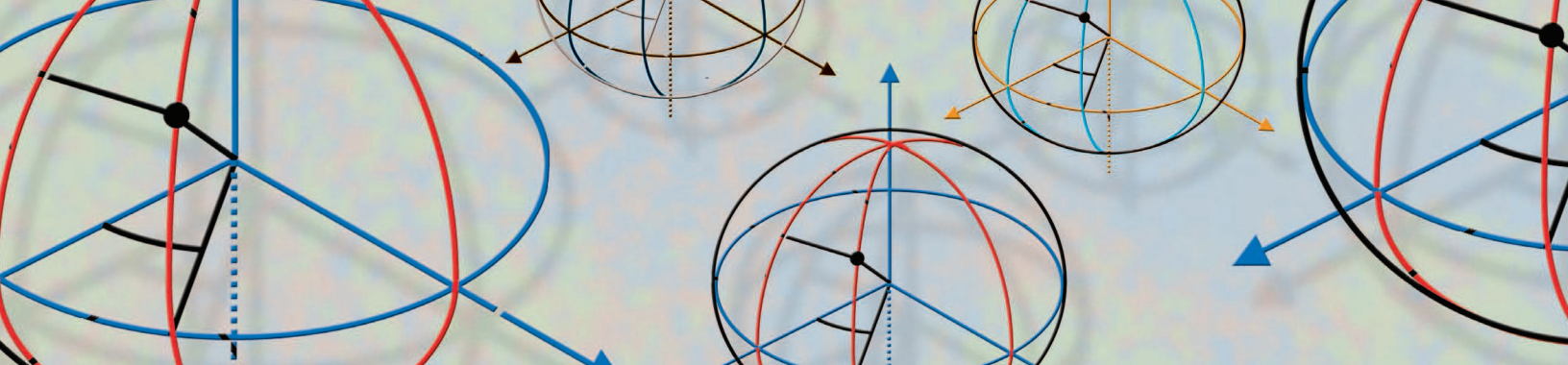


Fig. 1.

Simple accelerometer. (From [3] © Paul Groves 2013. Reproduced with permission.)

eration when the specific force is equal to and opposite of the acceleration due to gravity, the reaction to gravity is sensed as weight.

An accelerometer measures the specific force of the accelerometer case with respect to inertial space, which does not accelerate or rotate with respect to the rest of the universe. An IMU containing a triad of accelerometers with mutually orthogonal sensitive axes measures the specific-force vector, \mathbf{f}_{ib}^b , where the subscript ib denotes measurement of the origin of the IMU body frame, b , with respect to an inertial frame, i , and the superscript b denotes that the components of the vector are resolved along the axes of the IMU body frame, which normally coincide with the sensitive axes of the constituent sensors (an exception is the skewed configuration; Section IX). The specific force may be expressed in terms of the inertially referenced acceleration, \mathbf{a}_{ib}^b , and the gravitational acceleration, \mathbf{g}_{ib}^b , using

$$\mathbf{f}_{ib}^b = \mathbf{a}_{ib}^b - \mathbf{g}_{ib}^b. \quad (1)$$

However, it is often more convenient to express the specific force in terms of the Earth-referenced acceleration, \mathbf{a}_{eb}^b . Thus,

$$\mathbf{f}_{ib}^b = \mathbf{a}_{eb}^b - \mathbf{g}_b^b, \quad (2)$$

where \mathbf{g}_b^b is the acceleration due to gravity, the sum of the gravitational acceleration and the outward centrifugal acceleration due to the Earth's rotation. Centrifugal acceleration is a pseudo-acceleration arising from the use of a rotating reference frame [3].

The accelerometer hardware shown in Fig. 1 is incomplete. The proof mass must be supported in the axes perpendicular to the sensitive axis, and damping is needed to limit oscillation of the proof mass. Practical accelerometers used for navigation follow either a pendulous or a vibrating-beam design.

In a pendulous accelerometer, the proof mass is attached to the case via a pendulous arm and hinge, forming a pendulum.

This leaves the proof mass free to move along the sensitive axis while supporting it in the other two axes. The hinge provides damping, which may be increased by filling the case with oil. In an open-loop pendulous accelerometer, one or two springs are used to transmit force from the case to the pendulum along the sensitive axis. However, the accuracy is limited by the pickoff resolution, nonlinearity of the spring, and variation in the direction of the sensitive axis as the pendulum moves. Precision pendulous accelerometers therefore use a closed-loop, or force-feedback, configuration, whereby a torquer maintains the pendulous arm at a constant position with respect to the case [4, 5]. The pickoff detects departures from the equilibrium position as the specific force changes, and the torquer is adjusted to return the pendulum to that position. Thus, the force exerted by the torquer, not the pickoff signal, is proportional to the specific force.

Higher performance pendulous accelerometers are mechanical. Different grades of performance are offered at different prices by varying the component quality. Microelectromechanical system (MEMS) technology enables small and light quartz and silicon sensors to be mass produced at low cost using etching techniques with several sensors on a single wafer, offering a lower cost, lower performance alternative [6]. MEMS sensors also exhibit much greater shock tolerance than conventional designs, enabling them to be used in gun-launched guided munitions [7].

In a vibrating-beam accelerometer (VBA), the proof mass is also mounted on a pendulous arm. However, it is supported along the sensitive axis by a vibrating beam, largely constraining its motion. When a force is applied to the accelerometer case along the sensitive axis, the beam pushes or pulls the proof mass, causing the beam to be compressed in the former case and stretched in the latter. This changes the resonant frequency of the beam. Therefore, by measuring this, the specific force along the sensitive axis can be determined. Performance is improved by using a pair of vibrating beams, arranged such that one is compressed while the other is stretched. Larger, higher performance VBAs use quartz, while lower cost MEMS VBAs can use quartz or silicon.

A third class of accelerometer, currently under development, is based on cold-atom interferometry [8, 9]. This offers a much higher precision than conventional sensors but is relatively large and expensive, limiting its deployment to larger ships, submarines, and aircraft.

The operating range of an accelerometer is typically quoted in terms of the acceleration due to gravity, abbreviated to g , where $1g = 9.80665 \text{ m s}^{-2}$ and the actual acceleration due to gravity varies with location. Many navigation applications require an operational range of at least $\pm 10g$.

B. GYROSCOPES

A device that senses angular rate with respect to inertial space is known as a gyro. Early gyros used spinning-mass technology. However, most gyros used for navigation today are either optical or vibratory. An IMU containing a triad of gyros with mutually orthogonal sensitive axes measures the angular-rate vector, ω_{ib}^b , where the subscript ib denotes measurement of the axes of the IMU body frame with respect to an inertial frame and the superscript b denotes that the components of the vector are resolved about the axes of the IMU body frame, which normally coincide with the gyro sensitive axes. Manned vehicles typically rotate at up to 3 rad s^{-1} (170° s^{-1}) [10]. However, a gun-launched guided shell can rotate at up to 120 rad s^{-1} ($6800^\circ \text{ s}^{-1}$) [7].

1) *Optical Gyros:* Optical gyros work on the principle that, in a given medium, light travels at a constant speed in an inertial frame. If light is sent in both directions around a nonrotating closed-loop waveguide made of mirrors or optical fiber, the path length is the same for both beams. However, if the waveguide is rotated within its plane, then from the perspective of an inertial frame, the reflecting surfaces are moving farther apart for light traveling in the same direction as the rotation and closer together for light traveling in the opposite direction. Thus, rotating the waveguide in the same direction as the light path increases the path length and rotating it in the opposite direction decreases the path length. This is known as the Sagnac effect and is illustrated by Fig. 2. By measuring the changes in path length, the angular rate of the waveguide with respect to inertial space can be determined.

There are two main types of optical gyros. The ring laser gyro (RLG) was originally designed as a high-performance technology, with the interferometric fiber-optic gyro (IFOG) as a lower cost solution. However, the performance ranges now overlap, with IFOGs able to meet the performance standards for civil and military aviation.

In a RLG, light travels in both directions around a closed-loop tube, known as a laser cavity, containing a helium–neon gas mixture. The cavity comprises at least three arms with a mirror at each corner. The wavelength of the light depends on both the properties of the gas and the length of the laser cavity, which must contain an integer number of wavelengths. If the laser cavity does not rotate, the light traveling in each direction

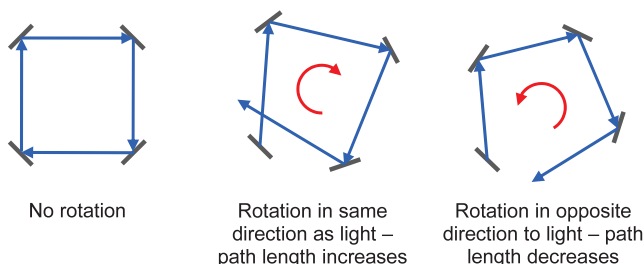


Fig. 2.

Effect of closed-loop waveguide rotation on path length. (From [3] © Paul Groves 2013. Reproduced with permission.)

has the same wavelength. However, if the laser cavity is rotated within its plane, the cavity length is increased for light traveling in the direction of rotation and decreased for the light traveling in the opposite direction, changing both wavelengths. Light traveling in both directions is focused on a detector, and the angular rate is deduced from the interference pattern.

In an IFOG, broadband light is modulated and split into two equal portions that are then sent through a fiber-optic coil in opposite directions. Within the coil, light traveling in one direction is lagged or advanced with respect to light traveling in the other direction according to the angular rate of the coil within its plane. The outputs from the coil are recombined and passed to a detector that measures the interference between them, from which the angular rate may be deduced.

2) *Vibratory Gyros:* A vibratory gyro is based around a driven vibrating element, which may be a string, beam, pair of beams, tuning fork, ring, cylinder, or hemisphere. The Coriolis acceleration of the vibrating element is detected when the gyro is rotated. Fig. 3 illustrates this for a vibrating string. This is able to vibrate in two orthogonal directions and is driven to vibrate along one of these directions. If the string is then rotated about its longitudinal axis, which is perpendicular to the directions it can vibrate along, the Coriolis effect induces vibration along the axis perpendicular to both the drive and the longitudinal axes. The amplitude of this vibration is proportional to the angular rate.

Most vibratory gyros are low-cost, low-performance devices, often using MEMS technology [6] and with quartz giving better performance than silicon. The exception is the hemispherical resonator gyro, which can offer aviation-grade performance and is often used for space applications.

3) *Other Types of Gyros:* Traditional spinning-mass gyros remain in use in old equipment, but a number of new technologies for sensing angular rate are under development. Nuclear magnetic resonance gyro technology has been developed on a chip scale, offering high performance with small and light sensors [11]. Cold-atom interferometry offers the potential of much higher precision than current gyro technology for large-scale applications [12]. In theory, angular rate can also be sensed using an array of accelerometers [13]. However, this is not a practical solution.

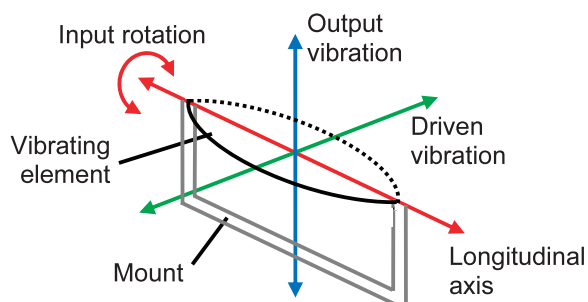


Fig. 3.

Axes of vibrating gyro.

C. INERTIAL MEASUREMENT UNITS

Fig. 4 shows the main elements of a typical IMU. The IMU regulates the power supplies to the accelerometers and gyros, digitizes their outputs, and transmits them on a data bus. The specific forces and angular rates, or their integrals (known as delta-v and delta-θ) are output at a rate between 100 and 1000 Hz. Most IMUs have three accelerometers and three gyros, mounted with orthogonal sensitive axes. However, some incorporate additional inertial sensors in a skewed configuration to protect against single-sensor failure (Section IX). Conversely, for some land vehicle applications, partial IMUs, comprising three accelerometers and a single yaw-axis gyro, are used [14].

Inertial sensors exhibit systematic errors (Section III) that can be calibrated in the laboratory and stored in memory, enabling the IMU processor to correct the sensor outputs. These errors vary with temperature, so the calibration is performed at a range of temperatures and the IMU is equipped with a temperature sensor.

Inertial sensors are sensitive to vibration (e.g., from a propulsion system). Many IMUs therefore incorporate vibration isolators, which also protect the components from shock. These must be designed to limit the transmission of vibrations at frequencies (and harmonics thereof) close to either the mechanical resonances of the sensors or the computational update rates of the IMU [4, 10].

There is no universally agreed upon definition of high-, medium-, and low-grade inertial sensors. One author's medium

grade can be another's high or low grade. IMUs, INSs, and inertial sensors may be grouped into five broad performance categories: marine, aviation, intermediate, tactical, and consumer.

The highest quality sensors are used in military ships, submarines, some intercontinental ballistic missiles, and some spacecraft, and different sensors are required for these different environments. A marine-grade INS can cost in excess of \$1 million.

Aviation- or navigation-grade INSs are used in military aircraft and commercial airliners. They cost around \$100 000, have a standard size of 178×178×249 mm, and must exhibit a horizontal position drift within 1.5 km in the first hour of operation. An intermediate-grade IMU, about an order of magnitude poorer in performance, is used in smaller aircraft and helicopters and costs \$20 000–\$50 000.

A tactical-grade IMU can only be used for a stand-alone INS for a few minutes. However, an accurate long-term navigation solution can be obtained by integrating it with a positioning system, such as the global positioning system (GPS). These IMUs typically cost between \$2 000 and \$30 000 and are used in guided weapons and unmanned air vehicles (UAVs). Most are less than a liter in volume. Tactical grade covers a wide span of sensor performance, particularly for gyros.

The lowest grade of inertial sensors is known as consumer or automotive grade. They are usually supplied as individual sensors or accelerometer and gyro triads, rather than as complete IMUs. Without calibration, they are not accurate enough for inertial navigation, even when integrated with other naviga-

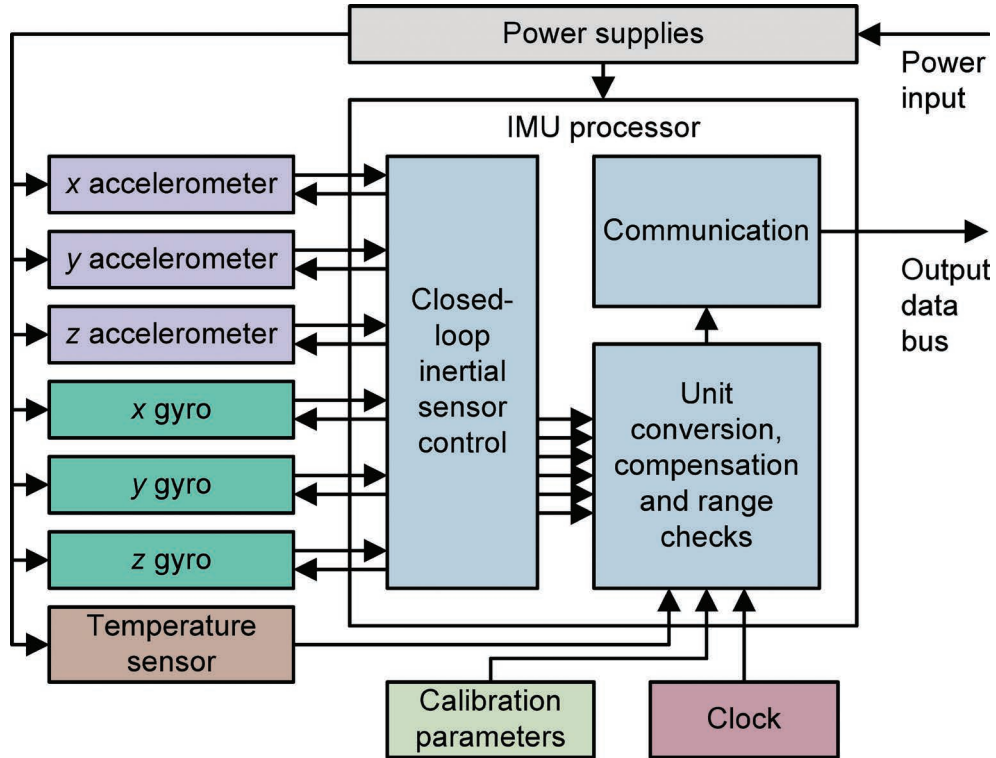


Fig. 4.

Schematic of IMU. (From [3] © Paul Groves 2013. Reproduced with permission.)

tion systems, but they can be used for attitude determination, detection of a pedestrian's steps, and detection of context information, such as vehicle type and activity. They are typically used in pedometers, antilock braking, active suspension, and airbags. Accelerometers cost around \$1 while gyro prices start around \$10. Sensors can be as small as $5 \times 5 \times 1$ mm.

The extent of calibration and other processing applied within the IMU can affect performance dramatically, particularly for MEMS sensors [15]. Sometimes, the same MEMS inertial sensors are sold at consumer grade without calibration and tactical grade with calibration.

III. SENSOR ERROR CHARACTERISTICS

All types of accelerometers and gyros exhibit biases, scale-factor and cross-coupling errors, and random noise to a certain extent. Further errors may also arise, depending on the sensor type. Each of these errors is discussed in turn, followed by a summary error model. Further details may be found in [3, 4, 10].

Each systematic error source has four components: a fixed contribution, a temperature-dependent variation, a run-to-run variation, and an in-run variation. The fixed contribution is present each time the sensor is used and is normally corrected by the IMU processor using the laboratory calibration data. The temperature-dependent component can be similarly corrected. Otherwise, the systematic errors typically vary over the first few minutes of operation as the sensor warms up to its normal operating temperature.

The run-to-run variation of each error source results in a contribution to the total error, which is different each time the sensor is used but remains constant within any run. The in-run variation contribution changes slowly during the course of a run. Neither can be corrected by the IMU processor, but they can be calibrated through integration with other navigation sensors, as described in Section VI. Sudden step changes in the systematic errors can also occur if an IMU is subject to a large shock, such as launching it from a gun [7].

In discussing the error performance of different types of inertial sensors here, the contributions to the error sources that are

corrected within the IMU are neglected because the postcalibration performance is of greatest interest.

A. BIASES

The bias is a constant error exhibited by all accelerometers and gyros. It is independent of the underlying specific force and angular rate and is usually the largest error source. Accelerometer biases are typically quoted in units of milli-g (mg) or micro-g (μg), where $1\text{g} = 9.80665 \text{ m s}^{-2}$. For gyro biases, degrees per hour ($^{\circ} \text{ h}^{-1}$) are normally used, where $1^{\circ} \text{ h}^{-1} = 4.848 \times 10^{-6} \text{ rad s}^{-1}$. Table 1 lists typical accelerometer and gyro biases for different grades of IMU [3].

Pendulous accelerometers span most of the performance range, while VBAs exhibit biases of 0.1 mg upward, with MEMS accelerometers of both types exhibiting the largest biases. RLG biases vary from 0.001 to $10^{\circ} \text{ h}^{-1}$, depending on the sensor quality, while IFOG biases range between 0.01 and $100^{\circ} \text{ h}^{-1}$ and vibratory-gyro biases range from 1° h^{-1} to 1° s^{-1} . Uncalibrated MEMS sensors can exhibit larger biases, including temperature variations of several degrees per second or milli-g [16].

B. SCALE-FACTOR AND CROSS-COUPLING ERRORS

The scale-factor error is the departure of the input-output gradient of the instrument from unity. The resulting accelerometer error is thus proportional to the true specific force, while the gyro error is proportional to the true angular rate. The lowest cost sensors can exhibit significant scale-factor asymmetry, whereby the scale-factor errors are different for positive and negative readings.

Cross-coupling errors make each accelerometer sensitive to the specific force along the axes orthogonal to its sensitive axis and each gyro sensitive to the angular rate about the axes orthogonal to its sensitive axis. One of the major causes is mounting misalignment, whereby the sensitive axes of the inertial sensors are not completely orthogonal because of manufacturing limitations. In vibratory sensors, cross-talk between individual sensors can arise. In consumer-grade MEMS sensors,

Table 1.

IMU grade	Accelerometer bias		Gyro bias	
	mg	m s^{-2}	$^{\circ} \text{ h}^{-1}$	rad s^{-1}
Marine	0.01	10^{-4}	0.001	5×10^{-9}
Aviation	0.03–0.1	3×10^{-4} – 10^{-3}	0.01	5×10^{-8}
Intermediate	0.1–1	10^{-3} – 10^{-2}	0.1	5×10^{-7}
Tactical	1–10	0.01–0.1	1–100	5×10^{-6} – 5×10^{-4}
Consumer	>3	>0.03	>100	> 5×10^{-4}

the cross-coupling errors of the sensor can dominate. Cross-coupling errors are sometimes called misalignment errors or cross-axis sensitivity.

Scale-factor and cross-coupling errors are typically expressed in parts per million (ppm) or as a percentage, though some manufacturers quote the axis misalignments instead. The scale-factor and cross-coupling errors of most types of inertial sensors, including IFOGs, are between 10^{-4} and 10^{-3} (100–1000 ppm). However, some uncalibrated consumer-grade MEMS sensors exhibit scale-factor errors as high as 0.1 (10%) and cross-coupling errors of up to 0.02 (2%), while RLG scale-factor errors are typically between 10^{-6} and 10^{-4} (1–100 ppm).

C. RANDOM NOISE

Accelerometers and gyros all exhibit random noise from both electrical and mechanical sources. This noise is approximately white for frequencies below 1 Hz, so the standard deviation of the average specific force and angular-rate noise varies in inverse proportion to the square root of the averaging time. Consequently, the noise is often described using the root power spectral density (PSD) with units of micrograms per the square root of a hertz ($=9.80665 \times 10^{-6} \text{ m s}^{-1.5}$) for accelerometer random noise and units of micrograms per the square root of an hour ($=2.909 \times 10^{-4} \text{ rad s}^{-0.5}$) for gyro random noise commonly used. The noise standard deviation is the corresponding root PSD multiplied by the square root of the sampling rate (or divided by the square root of the sampling interval). Thus, at a sampling rate of 400 Hz, an accelerometer noise PSD of $100 \mu\text{g}/\sqrt{\text{Hz}}$ corresponds to a noise standard deviation of 2 mg or 0.196 m s^{-2} . White random noise cannot be calibrated, because there is no correlation between past and future values. MEMS sensors can also exhibit significant high-frequency noise, which can cause problems under high dynamics or high vibration.

The accelerometer and gyro random noise are sometimes described as random walks. This is because random noise on the specific-force measurements is integrated to produce a random-walk error on the inertial velocity solution. Similarly, angular-rate random noise is integrated to produce an attitude random-walk error. The standard deviation of a random-walk process is proportional to the square root of the integration time.

The accelerometer random-noise root PSD varies from $\sim 20^\circ/\sqrt{\text{Hz}}$ for aviation-grade IMUs, through $\sim 100^\circ/\sqrt{\text{Hz}}$ for tactical-grade IMUs, and up to $\sim 1000^\circ/\sqrt{\text{Hz}}$ for consumer-grade MEMS sensors. Gyro random noise varies from $0.001\text{--}0.02^\circ/\sqrt{\text{h}}$ for RLGs, through $0.03\text{--}0.1^\circ/\sqrt{\text{h}}$ for tactical-grade IFOGs or quartz vibratory gyros, to $0.06\text{--}2^\circ/\sqrt{\text{h}}$ for MEMS silicon vibratory gyros. For consumer-grade sensors, many manufacturers quote the standard deviation of the total noise (white and high frequency) at the sensor output rate instead of the root PSD. Noise levels of 2.5–10 mg for accelerometers and $0.3\text{--}1^\circ \text{ s}^{-1}$ for gyros are common.

A further source of noise is the quantization of the IMU data-bus outputs. This rounds the sensor output to an integer multiple of a constant, known as the quantization level, as shown in Fig. 5. The quantization errors are largest for consumer-grade

sensors, where the word length is typically 12 bits or less and they can have an impact similar to the noise of the sensors. Thus, quantization errors can be as high as 10^{-3} m s^{-1} for integrated specific-force increments and $2 \times 10^{-5} \text{ rad}$ for attitude increments.

D. FURTHER ERROR SOURCES

Inertial sensors often exhibit nonlinearity, whereby the scale factor varies with the specific force or angular rate. This is normally expressed as the variation of the scale factor over the operating range of the sensor and ranges from 10^{-5} for some RLGs, through 10^{-4} to 10^{-3} for most inertial sensors, and to 10^{-2} for MEMS gyros. The largest nonlinearity effects typically occur at the maximum angular rates or specific forces that the sensor will measure.

Vibration interacts with the sensor scale-factor and cross-coupling errors to produce oscillating sensor errors, which largely average to zero over time. However, nonlinearity, asymmetry, or both of the scale-factor and cross-coupling errors results in a component of the vibration-induced sensor error that does not cancel. This is known as a vibration rectification error and behaves like a bias that varies with the amplitude of the vibration.

Further error characteristics can be exhibited by certain types of accelerometers and gyros. Vibratory gyros and some IFOGs exhibit a sensitivity to the specific force along all three axes, known as the *g*-dependent bias. The coefficient is of the order of $1^\circ \text{ h}^{-1} \text{ g}^{-1}$ ($4.944 \times 10^{-5} \text{ rad m}^{-1} \text{ s}$) for an IFOG and $10^\circ\text{--}200^\circ \text{ h}^{-1} \text{ g}^{-1}$ for an uncalibrated vibratory gyro [4]. Open-loop sensors, including some MEMS accelerometers and vibratory gyros, can also exhibit anisoinertia errors, whereby the cross-coupling errors vary as a function of the specific force or angular rate because of changes in the direction of the sensitive axis. These errors can interact with vibration in the environment to produce a biaslike error known as the vibropendulous error.

MEMS sensors often exhibit errors because their operating ranges are exceeded, in which case the sensor simply outputs its largest possible positive or negative reading. Human motion exceeds the maximum ranges of many consumer-grade sensors.

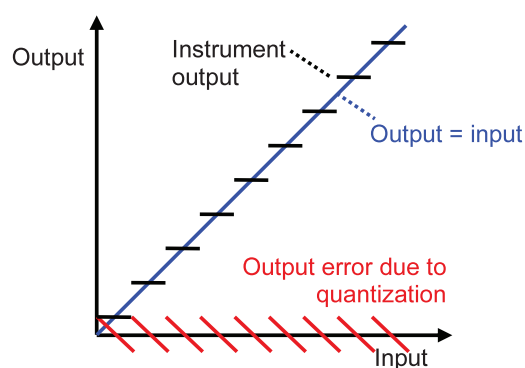


Fig. 5.

Effect of quantization on sensor output. (From [3] © Paul Groves 2013. Reproduced with permission.)

Errors can also arise when the bandwidth of the sensor is exceeded, particularly for high-vibration environments.

E. ERROR MODEL

The contribution of the main error sources to the outputs of an accelerometer triad may be summarized by

$$\tilde{\mathbf{f}}_{ib}^b = \mathbf{b}_a + (\mathbf{I}_3 + \mathbf{M}_a) \mathbf{f}_{ib}^b + \mathbf{w}_a, \quad (3)$$

where $\tilde{\mathbf{f}}_{ib}^b$ is the IMU-output specific-force vector, \mathbf{b}_a is the accelerometer bias vector, \mathbf{I}_3 is the identity matrix, \mathbf{M}_a is the matrix of coefficients of the accelerometer scale-factor error (diagonal elements) and cross-coupling error (off-diagonal elements), \mathbf{f}_{ib}^b is the true specific force, and \mathbf{w}_a is the accelerometer random-noise vector.

Similarly, for a gyro triad,

$$\tilde{\omega}_{ib}^b = \mathbf{b}_g + (\mathbf{I}_3 + \mathbf{M}_g) \omega_{ib}^b + \mathbf{G}_g \mathbf{f}_{ib}^b + \mathbf{w}_g, \quad (4)$$

where $\tilde{\omega}_{ib}^b$ is the IMU-output angular-rate vector, \mathbf{b}_g is the gyro bias vector, \mathbf{M}_g is the matrix of gyro scale-factor error and cross-coupling error coefficients, \mathbf{G}_g is the matrix of gyro g -dependent errors, ω_{ib}^b is the true angular rate, and \mathbf{w}_g is the gyro random-noise vector.

IV. STRAPDOWN INERTIAL NAVIGATION

As shown in Fig. 6, an INS comprises an IMU, described in Section II, and a navigation processor, which forms the focus of this section. The navigation processor computes a position, velocity, and attitude solution from the specific-force and angular-rate measurements made by the inertial sensors. For marine-, aviation-, and intermediate-grade systems, the IMU and navigation processor are typically packaged together. Where tactical- or consumer-grade sensors are used, the navigation equations are typically implemented on an integrated navigation processor or the application's central processor.

The section begins by introducing inertial navigation, going from a single-dimensional implementation through two dimensions to three, followed by a discussion of initialization. The navigation equations are then described, with a derivation of the simplest form followed by the presentation of a more precise set of equations. Further implementations are described in [3, 4, 17, 18], including those using integrated specific-force and attitude increments (Δv and $\Delta \theta$). The section concludes by describing error propagation.

A. INTRODUCTION TO INERTIAL NAVIGATION

Considering first an example of one-dimensional inertial navigation, a body, b , is constrained to move in a straight line perpendicular to the direction of gravity with respect to an Earth-fixed reference frame, p . The body's axes are fixed with respect to frame p , so it does not rotate. Its Earth-referenced accelera-

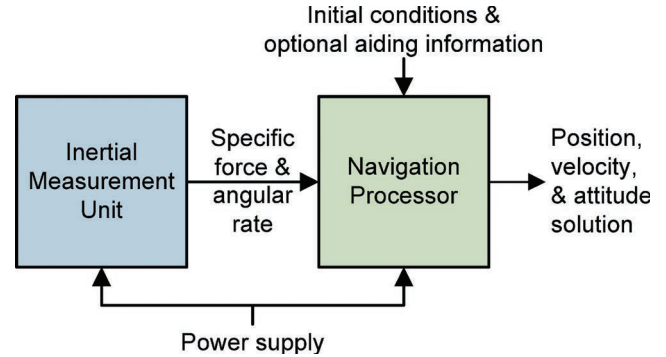


Fig. 6.

Basic schematic of an INS. (From [3] © Paul Groves 2013. Reproduced with permission.)

tion may be measured by a single accelerometer with its sensitive axis aligned along the direction of motion (neglecting the Coriolis force).

If the speed, v_{pb} , is known at an earlier time, t_0 , it may be determined at a later time, t , simply by integrating the acceleration, a_{pb} :

$$v_{pb}(t) = v_{pb}(t_0) + \int_{t_0}^t a_{pb}(t') dt'. \quad (5)$$

Similarly, the position may be obtained by integrating the velocity:

$$\begin{aligned} r_{pb}(t) &= r_{pb}(t_0) + \int_{t_0}^t v_{pb}(t') dt' \\ &= r_{pb}(t_0) + (t - t_0)v_{pb}(t_0) + \int_{t_0}^t \int_{t_0}^{t'} a_{pb}(t'') dt'' dt' \end{aligned} \quad . \quad (6)$$

Moving on to a two-dimensional example, b is now constrained to move within a horizontal plane defined by the x and y axes of the p frame. It may be oriented in any direction within this plane but is constrained to remain level. It thus has one angular and two linear degrees of freedom. Following the one-dimensional example, the position and velocity, resolved along the axes of reference frame p are updated using

$$\begin{pmatrix} v_{pb,x}^p(t) \\ v_{pb,y}^p(t) \end{pmatrix} = \begin{pmatrix} v_{pb,x}^p(t_0) \\ v_{pb,y}^p(t_0) \end{pmatrix} + \int_{t_0}^t \begin{pmatrix} a_{pb,x}^p(t') \\ a_{pb,y}^p(t') \end{pmatrix} dt', \quad (7)$$

$$\begin{pmatrix} x_{pb}^p(t) \\ y_{pb}^p(t) \end{pmatrix} = \begin{pmatrix} x_{pb}^p(t_0) \\ y_{pb}^p(t_0) \end{pmatrix} + \int_{t_0}^t \begin{pmatrix} v_{pb,x}^p(t') \\ v_{pb,y}^p(t') \end{pmatrix} dt'. \quad (8)$$

Measuring the acceleration along two orthogonal axes requires two accelerometers. However, their sensitive axes will be aligned with those of the body b . To determine the acceleration along the axes of frame p , the heading of body b with respect to frame p , ψ_{pb} , is required as shown in Fig. 7. The resolving axes of the accelerometer measurements may be then be transformed using a 2×2 coordinate transformation matrix:

$$\begin{pmatrix} a_{pb,x}^p(t') \\ a_{pb,y}^p(t') \end{pmatrix} = \begin{pmatrix} \cos\psi_{pb}(t') & -\sin\psi_{pb}(t') \\ \sin\psi_{pb}(t') & \cos\psi_{pb}(t') \end{pmatrix} \begin{pmatrix} a_{pb,x}^b(t') \\ a_{pb,y}^b(t') \end{pmatrix}. \quad (9)$$

The rotation of body b within the xy plane of reference frame p may be measured with a single gyro with its sensitive axis perpendicular to the plane (neglecting Earth rotation). If heading ψ_{pb} is known at the earlier time t_0 , it may be determined at the later time t by integrating the angular rate measured by the gyro, $\omega_{pb,z}^b$:

$$\psi_{pb}(t) = \psi_{pb}(t_0) + \int_{t_0}^t \omega_{pb,z}^b(t') dt'. \quad (10)$$

Three inertial sensors are thus required to measure the three degrees of freedom of motion in two dimensions.

For all practical applications, three-dimensional motion must be assumed. Even for land and marine navigation, strap-down inertial sensors will not remain in the horizontal plane because of terrain slopes or ship pitching and rolling. Consequently, nominally horizontal accelerometers will sense the reaction to gravity, as well as the horizontal-plane acceleration. A platform tilt of 10 mrad (0.57°) produces an acceleration error of 0.1 m s⁻², leading to a position error 500 m after 100 s (Section IV.E). Tilts of 10 times this are commonly exhibited by both cars and boats.

Unconstrained motion in three dimensions has six degrees of freedom, three linear and three angular, requiring six inertial sensors to measure it. The specific force, \mathbf{f}_{ib}^b , and angular rate, $\boldsymbol{\omega}_{ib}^b$, output by the IMU are integrated to produce an updated position, velocity, and attitude solution in four steps:

1. The attitude update
2. The transformation of the specific-force resolving axes from the IMU body frame to the coordinate frame used to resolve the position and velocity
3. The velocity update, including transformation of specific force into acceleration using a gravity or gravitation model
4. The position update

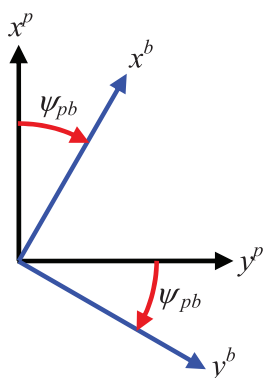


Fig. 7.

Orientation of body axes with respect to resolving axes in horizontal plane. (From [3] © Paul Groves 2013. Reproduced with permission.)

Further details are presented in Sections IV.C and IV.D. Fig. 8 summarizes this process. The specific force and angular rate from the IMU are averaged over its sampling interval, whereas the position, velocity, and attitude are applicable at the end of this interval. In an integrated navigation system, there may also be correction of the IMU outputs and navigation solution using estimates from the integration algorithm (Section VI.E). Where a partial IMU is used, the missing angular-rate measurements are assumed to be zero.

B. INITIALIZATION

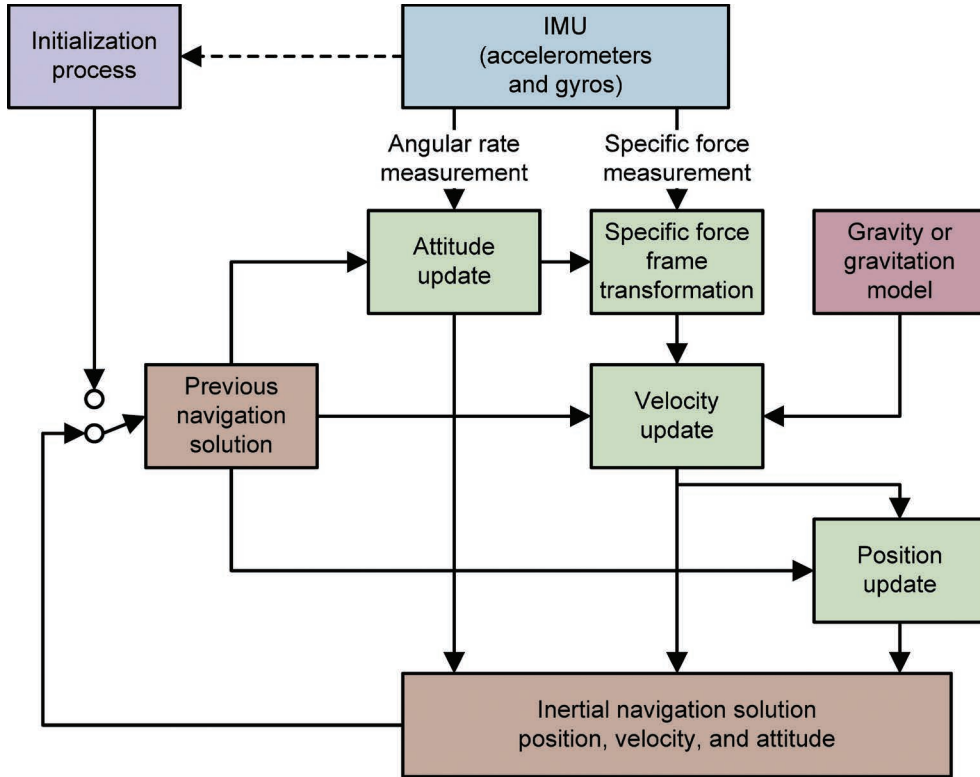
As Fig. 8 shows, each cycle of the inertial navigation equations uses the previous navigation solution as its starting point. Therefore, the position, velocity, and attitude solution must be initialized. Position and velocity initialization requires external information. The position can be initialized by starting at a known position. However, when inertial navigation forms part of an integrated navigation system (Section VI), another navigation technology, such as global navigation satellite systems (GNSSs), is commonly used to initialize position.

Velocity may also be initialized from another navigation system. However, it is common to set it to zero (with respect to the Earth) when the host vehicle is stationary. The effects of disturbance by wind or human activity, such as refueling and loading, may be minimized by performing the initialization process over several seconds, averaging out the motion effects.

When an INS is stationary, it can initialize its own attitude solution, a process known as self-alignment. The roll and pitch components of attitude are determined by measuring the direction of gravity using the accelerometers, a process known as leveling and described in Section V.A. The heading may be determined by measuring the rotation of the Earth using the gyros, which is known as gyrocompassing and described in Section V.B. However, effective gyrocompassing requires sensors of aviation grade or better. Otherwise, the heading must be initialized using external information. A magnetic heading measurement is described in Section V.C. Other methods, described in [3], include GNSS interferometric attitude determination, heading from trajectory, and image-based techniques.

C. SIMPLE INERTIAL-FRAME NAVIGATION EQUATIONS

The simplest form of the inertial navigation equations computes a position, velocity, and attitude with respect to, and resolved along the axes of, an Earth-centered inertial (ECI) coordinate frame. An ECI frame, denoted i , is an inertial frame with its origin at the Earth's center of mass. The z axis points along the Earth's axis of rotation from the origin to the true north pole. The x and y axes lie within the equatorial plane but do not rotate with the Earth. The y axis points 90° ahead of the x axis in the direction of the Earth's rotation. An ECI-frame implementation is simplest because the inertial sensors measure motion with respect to an inertial frame, so only two coordinate frames,

**Fig. 8.**

Schematic of inertial navigation processor. (From [3] © Paul Groves 2013. Reproduced with permission.)

the ECI frame and the body frame, are used. The effects of the Earth's rotation need not be considered. However, for most applications, the inertially referenced navigation solution must be transformed to an Earth-referenced solution to be useful.

The four steps, described in turn in this subsection, show how the angular-rate and specific-force measurements made over the time interval t to $t + \tau_i$ are used to update the navigation solution. The suffixes (−) and (+) are, respectively, used to denote values at the beginning of the navigation equations processing cycle, at time t , and at the end of the processing cycle, at time $t + \tau_i$.

1) *Attitude Update:* The attitude update step of the inertial navigation equations uses the angular-rate measurement from the IMU, ω_{ib}^b , to update the attitude solution, expressed as the body-to-inertial frame coordinate transformation matrix, \mathbf{C}_b^i . A coordinate transformation matrix, also known as a rotation matrix, is used to transform a vector from one set of resolving axes to another. Thus, for an arbitrary vector, \mathbf{x} ,

$$\mathbf{x}^i = \mathbf{C}_b^i \mathbf{x}^b, \quad (11)$$

where the superscript of \mathbf{x} denotes the resolving axes. The lower index of the coordinate transformation matrix represents the “from” frame, and the upper index represents the “to” frame. Transformations are reversed simply by transposing the matrix; thus,

$$\mathbf{C}_i^b = \mathbf{C}_b^{i\top}.$$

To perform successive transformations or rotations, the coordinate transformation matrices are simply multiplied:

$$\mathbf{C}_a^i = \mathbf{C}_b^i \mathbf{C}_a^b. \quad (12)$$

However, as with any matrix multiplication, the order is critical, so $\mathbf{C}_a^i \neq \mathbf{C}_a^b \mathbf{C}_b^i$. Performing a transformation and then reversing the process must return the original vector or matrix, so

$$\mathbf{C}_i^b \mathbf{C}_b^i = \mathbf{I}_3, \quad (13)$$

where \mathbf{I}_n is the $n \times n$ identity or unit matrix. Coordinate transformation matrices are thus orthonormal and only three of the nine components are independent. Although not always the most computationally efficient way of representing attitude, coordinate transformation matrices are comparatively straightforward and intuitive to manipulate.

As shown in [3, 19], the time derivative of the coordinate transformation matrix is

$$\dot{\mathbf{C}}_b^i = \mathbf{C}_b^i \boldsymbol{\Omega}_{ib}^b, \quad (14)$$

where $\boldsymbol{\Omega}_{ib}^b$ is the skew-symmetric matrix of the angular rate, defined as

$$\boldsymbol{\Omega}_{ib}^b = [\boldsymbol{\omega}_{ib}^b \wedge] = \begin{pmatrix} 0 & -\omega_{ib,z}^b & \omega_{ib,y}^b \\ \omega_{ib,z}^b & 0 & -\omega_{ib,x}^b \\ -\omega_{ib,y}^b & \omega_{ib,x}^b & 0 \end{pmatrix}. \quad (15)$$

Integrating (14) over the inertial navigation update interval gives

$$\mathbf{C}_b^i(t + \tau_i) = \mathbf{C}_b^i(t) \left[\lim_{n \rightarrow \infty} \prod_{i=1}^n \exp \left(\boldsymbol{\Omega}_{ib}^b \left(t + \frac{n-i}{n} \tau_i \right) \frac{\tau_i}{n} \right) \right]. \quad (16)$$

If the angular rate is assumed to be constant over this interval, this simplifies to

$$\begin{aligned} \mathbf{C}_b^i(t + \tau_i) &\approx \mathbf{C}_b^i(t) \exp(\boldsymbol{\Omega}_{ib}^b \tau_i) \\ &= \mathbf{C}_b^i(t) \exp([\boldsymbol{\omega}_{ib}^b \wedge] \tau_i). \\ &= \mathbf{C}_b^i(t) \exp[(\boldsymbol{\omega}_{ib}^b \tau_i) \wedge] \end{aligned} \quad (17)$$

The exponent of a matrix is not the same as the matrix of the exponents of its components. Expressing (17) as a power series,

$$\mathbf{C}_b^i(t + \tau_i) = \mathbf{C}_b^i(t) \sum_{r=0}^{\infty} \frac{[(\boldsymbol{\omega}_{ib}^b \tau_i) \wedge]^r}{r!}. \quad (18)$$

The simplest form of attitude update is obtained by truncating the power series to first order:

$$\begin{aligned} \mathbf{C}_b^i(+)&\approx \mathbf{C}_b^i(-) \left(\mathbf{I}_3 + [(\boldsymbol{\omega}_{ib}^b \tau_i) \wedge] \right) \\ &= \mathbf{C}_b^i(-) \left(\mathbf{I}_3 + \boldsymbol{\Omega}_{ib}^b \tau_i \right) \\ &= \mathbf{C}_b^i(-) \begin{pmatrix} 1 & -\omega_{ib,z}^b \tau_i & \omega_{ib,y}^b \tau_i \\ \omega_{ib,z}^b \tau_i & 1 & -\omega_{ib,x}^b \tau_i \\ -\omega_{ib,y}^b \tau_i & \omega_{ib,x}^b \tau_i & 1 \end{pmatrix} \end{aligned} \quad (19)$$

This first-order approximation of (18) is a form of the small angle approximation, $\sin \theta \approx \theta$, $\cos \theta \approx 1$. It introduces errors in the attitude integration that are larger at lower update rates (large τ_i) and higher angular rates. In practice, the first-order approximation can be used for land vehicle applications where the dynamics are low. However, for applications with high-dynamic motion, such as aviation, or regular periodic motion, such as pedestrian and boat navigation, a more precise attitude update is required, incorporating higher order terms in the power series; see (18).

2) *Specific-Force Frame Transformation*: The IMU measures specific force along the body-frame resolving axes. However, to use this to update the velocity solution, it must be resolved about the same axes as the velocity—in this case, an ECI frame. The resolving axes are transformed simply by applying a coordinate transformation matrix:

$$\mathbf{f}_{ib}^i(t) = \mathbf{C}_b^i(t) \mathbf{f}_{ib}^b(t). \quad (20)$$

Because the specific-force measurement is an average over time t to $t + \tau_i$, the coordinate transformation matrix should be similarly averaged. A good approximation is

$$\mathbf{f}_{ib}^i \approx \frac{1}{2} (\mathbf{C}_b^i(-) + \mathbf{C}_b^i(+)) \mathbf{f}_{ib}^b.$$

3) *Velocity Update*: From (1), inertially referenced acceleration is obtained by adding the gravitational acceleration to the specific force:

$$\mathbf{a}_{ib}^i = \mathbf{f}_{ib}^i + \boldsymbol{\gamma}_{ib}^i. \quad (21)$$

The gravitational acceleration is determined using a model [20]:

$$\boldsymbol{\gamma}_{ib}^i = -\frac{\mu}{|\mathbf{r}_{ib}^i|^3} \left\{ \mathbf{r}_{ib}^i + \frac{3}{2} J_2 \frac{R_0^2}{|\mathbf{r}_{ib}^i|^2} \left\{ \begin{aligned} &\left[1 - 5 \left(r_{ib,z}^i / |\mathbf{r}_{ib}^i| \right)^2 \right] r_{ib,x}^i \\ &\left[1 - 5 \left(r_{ib,z}^i / |\mathbf{r}_{ib}^i| \right)^2 \right] r_{ib,y}^i \\ &\left[3 - 5 \left(r_{ib,z}^i / |\mathbf{r}_{ib}^i| \right)^2 \right] r_{ib,z}^i \end{aligned} \right\} \right\}, \quad (22)$$

where \mathbf{r}_{ib}^i is the Cartesian position of the IMU body frame with respect to the ECI-frame origin, resolved along the ECI-frame axes; $R_0 = 6378137.0$ m is the Earth's equatorial radius; $\mu = 3.986004418 \times 10^{14}$ m³ s⁻² is the Earth's gravitational constant; and $J_2 = 1.082627 \times 10^{-3}$ is the Earth's second gravitational constant [21].

The time derivative of the velocity of the IMU body frame with respect to the ECI-frame origin, resolved along the ECI-frame axes, \mathbf{v}_{ib}^i , is simply the corresponding acceleration because the reference frame and resolving axes are the same. Thus,

$$\dot{\mathbf{v}}_{ib}^i = \mathbf{a}_{ib}^i. \quad (23)$$

The velocity is updated by integrating this. Assuming the acceleration is constant over the update interval gives

$$\mathbf{v}_{ib}^i(+) = \mathbf{v}_{ib}^i(-) + \mathbf{a}_{ib}^i \tau_i. \quad (24)$$

4) *Position Update*: As the reference frame and resolving axes are the same, the time derivative of the Cartesian position is simply the velocity. Thus,

$$\dot{\mathbf{r}}_{ib}^i = \mathbf{v}_{ib}^i. \quad (25)$$

Where the variation in acceleration over the update interval is unknown, \mathbf{v}_{ib}^i is assumed to be a linear function of time over the interval t to $t + \tau_i$. The position may therefore be updated using

$$\mathbf{r}_{ib}^i(+) = \mathbf{r}_{ib}^i(-) + (\mathbf{v}_{ib}^i(-) + \mathbf{v}_{ib}^i(+)) \frac{\tau_i}{2}. \quad (26)$$

5) *Navigation Solution Transformation*: To obtain a navigation solution with respect to the Earth, a transformation is required. An Earth-centered, Earth-fixed (ECEF) coordinate frame, denoted e , has its origin at the Earth's center of mass, coincident with the ECI-frame origin. The z axis also points from

the origin to the true north pole. However, the x and y axes are fixed with respect to the Earth, rotating with it, with the x and y axes pointing from the origin to the 0° and 90° east meridians, respectively. The Cartesian ECEF position is obtained using

$$\mathbf{r}_{eb}^e = \mathbf{C}_i^e \mathbf{r}_{ib}^i, \quad \mathbf{C}_i^e = \begin{pmatrix} \cos \omega_{ie}(t-t_0) & \sin \omega_{ie}(t-t_0) & 0 \\ -\sin \omega_{ie}(t-t_0) & \cos \omega_{ie}(t-t_0) & 0 \\ 0 & 0 & 1 \end{pmatrix}, \quad (27)$$

where t_0 is the time at which the ECEF-frame and ECI-frame axes coincide and $\omega_{ie} = 7.292115 \times 10^{-5}$ rad s $^{-1}$ is the Earth rotation rate [21].

For most applications, it is more convenient to express position with respect to the surface of the Earth rather than the center. The surface is irregular, so for navigation purposes, is typically approximated by an ellipsoid. The geodetic latitude of body b , L_b , is defined as the angle of intersection of the normal from b to the ellipsoid with the equatorial plane. The longitude, λ_b , is the angle subtended in the equatorial plane between the meridian plane containing b and the 0° meridian plane. Finally, the geodetic height, h_b , is the distance from b to the ellipsoid surface along the normal to that ellipsoid. Fig. 9 illustrates this. Together, L_b , λ_b , and h_b form the curvilinear position of body or point b . This may be determined from the corresponding Cartesian position using [22]:

$$\begin{aligned} \tan L_b &\approx \frac{z_{eb}^e \sqrt{1-e^2} + e^2 R_0 \sin^3 \zeta_b}{\sqrt{1-e^2} \left(\sqrt{x_{eb}^{e2} + y_{eb}^{e2}} - e^2 R_0 \cos^3 \zeta_b \right)} \\ \tan \lambda_b &= \frac{y_{eb}^e}{x_{eb}^e}, \\ h_b &= \frac{\sqrt{x_{eb}^{e2} + y_{eb}^{e2}}}{\cos L_b} - R_E(L_b) \end{aligned}, \quad (28)$$

where $e = 0.0818191908425$ [21] is the eccentricity of the ellipsoid and

$$\tan \zeta_b = \frac{z_{eb}^e}{\sqrt{1-e^2} \sqrt{x_{eb}^{e2} + y_{eb}^{e2}}}, \quad R_E(L_b) = \frac{R_0}{\sqrt{1-e^2 \sin^2 L_b}}, \quad (29)$$

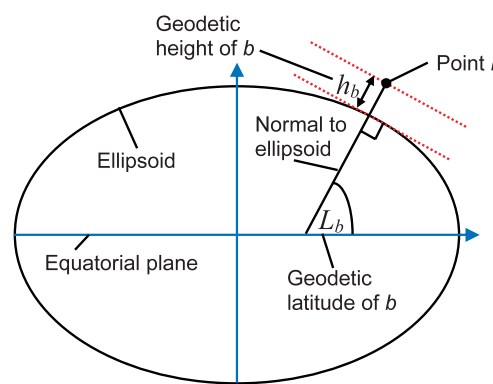


Fig. 9.
Geodetic latitude, longitude, and geodetic height of point b .

where R_E is the transverse radius of curvature.

The velocity with respect to the Earth, resolved along the north, east, and down (NED), an example of a local navigation frame, is obtained using [3]

$$\mathbf{v}_{eb}^n = \mathbf{C}_e^n \mathbf{C}_i^e \left(\mathbf{v}_{ib}^i - \boldsymbol{\Omega}_{ie}^i \mathbf{r}_{ib}^i \right), \quad (30)$$

where

$$\begin{aligned} \mathbf{C}_e^n &= \begin{pmatrix} -\sin L_b \cos \lambda_b & -\sin L_b \sin \lambda_b & \cos L_b \\ -\sin \lambda_b & \cos \lambda_b & 0 \\ -\cos L_b \cos \lambda_b & -\cos L_b \sin \lambda_b & -\sin L_b \end{pmatrix}, \\ \boldsymbol{\Omega}_{ie}^i &= \begin{pmatrix} 0 & -\omega_{ie} & 0 \\ \omega_{ie} & 0 & 0 \\ 0 & 0 & 0 \end{pmatrix}. \end{aligned} \quad (31)$$

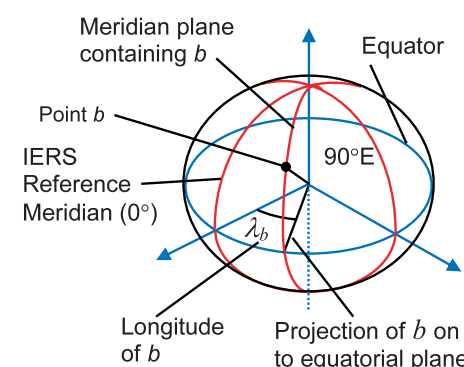
Finally, the attitude, expressed as the coordinate transformation matrix from the body frame to NED, is obtained using

$$\mathbf{C}_b^n = \mathbf{C}_e^n \mathbf{C}_i^e \mathbf{C}_b^i. \quad (32)$$

For user output, it is more intuitive to express attitude as a set of three Euler angles. The Euler attitude of the body frame with respect to NED may be expressed as a set of three rotations from NED to the body. First, the yaw rotation, ψ_{nb} , is a positive rotation about the z (down) axis of the NED frame. Second, the pitch rotation, θ_{nb} , is a positive rotation about the y (right) axis of the first intermediate frame. Finally, the roll rotation, ϕ_{nb} , is a positive rotation about the x (forward) axis of the second intermediate frame. The Euler angles may be obtained from the coordinate transformation matrix using

$$\begin{aligned} \phi_{nb} &= \arctan_2(C_{b3,2}^n, C_{b3,3}^n) \\ \theta_{nb} &= -\arcsin C_{b3,1}^n \\ \psi_{nb} &= \arctan_2(C_{b2,1}^n, C_{b1,1}^n) \end{aligned}, \quad (33)$$

where four-quadrant arctangent functions must be used. The reverse transformation is



$$\mathbf{C}_b^n = \mathbf{C}_n^{bT} = \begin{bmatrix} \cos\theta_{nb} \cos\psi_{nb} & \begin{pmatrix} -\cos\phi_{nb} \sin\psi_{nb} \\ +\sin\phi_{nb} \sin\theta_{nb} \cos\psi_{nb} \end{pmatrix} & \begin{pmatrix} \sin\phi_{nb} \sin\psi_{nb} \\ +\cos\phi_{nb} \sin\theta_{nb} \cos\psi_{nb} \end{pmatrix} \\ \cos\theta_{nb} \sin\psi_{nb} & \begin{pmatrix} \cos\phi_{nb} \cos\psi_{nb} \\ +\sin\phi_{nb} \sin\theta_{nb} \sin\psi_{nb} \end{pmatrix} & \begin{pmatrix} -\sin\phi_{nb} \cos\psi_{nb} \\ +\cos\phi_{nb} \sin\theta_{nb} \sin\psi_{nb} \end{pmatrix} \\ -\sin\theta_{nb} & \sin\phi_{nb} \cos\theta_{nb} & \cos\phi_{nb} \cos\theta_{nb} \end{bmatrix}. \quad (34)$$

D. PRECISION NED NAVIGATION EQUATIONS

The inertial navigation equations presented in the preceding subsection are approximate and exhibit errors that increase with the host-vehicle dynamics, vibration level, and update interval. For most applications, a higher precision, and thus greater complexity and processing capacity, is required. It is also common to directly compute an Earth-referenced navigation solution resolved about NED axes (or east, north, and up) instead of computing an ECI solution and converting. In such an implementation, it is necessary to account for the rotation of the Earth with respect to inertial space, including the ensuing Coriolis force, and the rotation of the NED coordinate frame with respect to the Earth as the navigation system moves. A derivation and explanation of the constituent terms may be found in [3, 4].

The attitude solution is updated using

$$\mathbf{C}_b^n(+) \approx \mathbf{C}_b^n(-)\mathbf{C}_{b+}^{b-} - (\boldsymbol{\Omega}_{ie}^n(-) + \boldsymbol{\Omega}_{en}^n(-))\mathbf{C}_b^n(-)\tau_i, \quad (35)$$

where, from (16), the rotation measured by the gyros is

$$\mathbf{C}_{b+}^{b-} = \mathbf{I}_3 + \frac{\sin|\boldsymbol{\omega}_{ib}^b \tau_i|}{|\boldsymbol{\omega}_{ib}^b \tau_i|} [\mathbf{(\omega}_{ib}^b \tau_i) \wedge] + \frac{1-\cos|\boldsymbol{\omega}_{ib}^b \tau_i|}{|\boldsymbol{\omega}_{ib}^b \tau_i|^2} [\mathbf{(\omega}_{ib}^b \tau_i) \wedge]^2, \quad (36)$$

the skew symmetric matrix of the angular rate of the Earth resolved about NED is

$$\boldsymbol{\Omega}_{ie}^n = \omega_{ie} \begin{pmatrix} 0 & \sin L_b & 0 \\ -\sin L_b & 0 & -\cos L_b \\ 0 & \cos L_b & 0 \end{pmatrix}, \quad (37)$$

and the skew symmetric matrix of the angular rate of the NED axes with respect to the Earth, known as the transport rate, is

$$\boldsymbol{\Omega}_{en}^n = \begin{pmatrix} 0 & -\omega_{en,z}^n & \omega_{en,y}^n \\ \omega_{en,z}^n & 0 & -\omega_{en,x}^n \\ -\omega_{en,y}^n & \omega_{en,x}^n & 0 \end{pmatrix}, \quad (38)$$

$$\boldsymbol{\omega}_{en}^n = \begin{pmatrix} v_{eb,E}^n / (R_E(L_b) + h_b) \\ -v_{eb,N}^n / (R_N(L_b) + h_b) \\ -v_{eb,E}^n \tan L_b / (R_E(L_b) + h_b) \end{pmatrix}$$

where

$$R_N(L_b) = \frac{R_0(1-e^2)}{(1-e^2 \sin^2 L_b)^{3/2}} \quad (39)$$

is the meridian radius of curvature. The attitude solution may be converted to Euler angles using (33). The coordinate transformation matrix should also be subject to a reorthogonalization and renormalization process at regular intervals to compensate for computational rounding errors [3, 4].

The specific-force resolving axes are transformed to NED using

$$\mathbf{f}_{ib}^n = \bar{\mathbf{C}}_b^n \mathbf{f}_{ib}^b, \quad \bar{\mathbf{C}}_b^n = \mathbf{C}_b^n(-) \mathbf{C}_{\bar{b}}^{b-} - \frac{1}{2} (\boldsymbol{\Omega}_{ie}^n(-) + \boldsymbol{\Omega}_{en}^n(-)) \mathbf{C}_b^n(-) \tau_i, \quad (40)$$

where

$$\mathbf{C}_{\bar{b}}^{b-} = \mathbf{I}_3 + \frac{1-\cos|\boldsymbol{\omega}_{ib}^b \tau_i|}{|\boldsymbol{\omega}_{ib}^b \tau_i|^2} [\mathbf{(\omega}_{ib}^b \tau_i) \wedge] + \frac{1}{|\boldsymbol{\omega}_{ib}^b \tau_i|^2} \left(1 - \frac{\sin|\boldsymbol{\omega}_{ib}^b \tau_i|}{|\boldsymbol{\omega}_{ib}^b \tau_i|} \right) [\mathbf{(\omega}_{ib}^b \tau_i) \wedge]^2. \quad (41)$$

The velocity solution is then updated using

$$\mathbf{v}_{eb}^n(+) \approx \mathbf{v}_{eb}^n(-) + \left[\mathbf{f}_{ib}^n + \mathbf{g}_{ib}^n(L_b(-), h_b(-)) - (\boldsymbol{\Omega}_{en}^n(-) + 2\boldsymbol{\Omega}_{ie}^n(-)) \mathbf{v}_{eb}^n(-) \right] \tau_i, \quad (42)$$

where the acceleration due to gravity is given by [21]:

$$\begin{aligned} g_{b,D}^n(L_b, h_b) &\approx g_0(L_b) \left\{ 1 - \frac{2}{R_0} \left[1 + f(1 - 2 \sin^2 L_b) + \frac{\omega_{ie}^2 R_0^2 R_p}{\mu} \right] h_b + \frac{3}{R_0^2} h_b^2 \right\} \\ g_{b,N}^n(L_b, h_b) &\approx -8.08 \times 10^{-9} h_b \sin 2L_b \text{ m s}^{-2} \\ g_0(L_b) &\approx 9.7803253359 \frac{(1 + 0.001931853 \sin^2 L_b)}{\sqrt{1 - e^2 \sin^2 L_b}} \text{ m s}^{-2} \end{aligned}, \quad (43)$$

where $f = 1/298.257223563$ is the flattening of the ellipsoid.

The curvilinear position may be updated directly from the velocity using

$$\begin{aligned} h_b(+) &= h_b(-) - \frac{\tau_i}{2} (v_{eb,D}^n(-) + v_{eb,D}^n(+)) \\ L_b(+) &\approx L_b(-) + \frac{\tau_i}{2} \left(\frac{v_{eb,N}^n(-)}{R_N(L_b(-)) + h_b(-)} + \frac{v_{eb,N}^n(+)}{R_N(L_b(-)) + h_b(+)} \right) \\ \lambda_b(+) &= \lambda_b(-) + \frac{\tau_i}{2} \left(\frac{v_{eb,E}^n(-)}{(R_E(L_b(-)) + h_b(-)) \cos L_b(-)} + \frac{v_{eb,E}^n(+)}{(R_E(L_b(+)) + h_b(+)) \cos L_b(+)} \right) \end{aligned}. \quad (44)$$

The preceding equations should be updated at the IMU output rate. However, it is possible to implement slower varying terms, such as the Earth rotation and transport rate contributions, at a lower rate, reducing processor load at the expense of increased complexity [23]. In addition, a NED-resolved implementation is not suitable for use in polar regions because north and east are undefined at the poles; an ECI-frame, ECEF-frame, or wander-azimuth implementation must be used instead [3, 17]. A wander-azimuth coordinate frame is a local-level frame in which the x and y axes are rotated about the vertical with

respect to north and east by a wander angle that varies with position, avoiding the singularity at the poles.

E. INS ERROR PROPAGATION

The errors in an INS arise from three sources: the inertial sensors, initialization errors, and processing approximations, including the gravity model. These errors are integrated through the navigation equations to produce position, velocity, and attitude errors that grow with time. For example, the velocity initialization error results in a growing position error. The error propagation is also affected by the host-vehicle trajectory. For example, the effect of scale-factor and cross-coupling errors depends on the host-vehicle dynamics, as does the coupling of the attitude errors, particularly heading, into velocity and position.

Full determination of INS error propagation is a complex problem, normally studied using simulation software. This section begins by defining the INS errors. Several examples of short-term error propagation are then presented, followed by brief discussions of longer term error propagation, the effects of maneuvers, and indexed IMUs. The Earth-referenced form of the navigation solution, resolved along NED, is used. A more detailed treatment of INS error propagation may be found in [4, 18, 20].

1) Error Definitions: In general, an INS error is simply the difference between an INS-indicated quantity, denoted by \sim , and the true value of that quantity. Thus, the Cartesian position, velocity and acceleration errors are

$$\begin{aligned}\delta\mathbf{r}_{eb}^n &= \tilde{\mathbf{r}}_{eb}^n - \mathbf{r}_{eb}^n \\ \delta\mathbf{v}_{eb}^n &= \tilde{\mathbf{v}}_{eb}^n - \mathbf{v}_{eb}^n \\ \delta\mathbf{a}_{eb}^n &= \tilde{\mathbf{a}}_{eb}^n - \mathbf{a}_{eb}^n.\end{aligned}\quad (45)$$

Similarly, the latitude, longitude, and height errors are

$$\begin{aligned}\delta L_b &= \tilde{L}_b - L_b \\ \delta\lambda_b &= \tilde{\lambda}_b - \lambda_b \\ \delta h_b &= \tilde{h}_b - h_b\end{aligned}\quad (46)$$

As explained in Section IV.C.1, coordinate transformation matrices are multiplied to perform successive transformations or rotations. Therefore, the attitude error in coordinate transformation matrix form is obtained by multiplying the attitude solution by the transpose of the true attitude:

$$\delta\mathbf{C}_b^n = \tilde{\mathbf{C}}_b^n \mathbf{C}_n^n. \quad (47)$$

The attitude error components are resolved about the axes of the NED frame. Where the small angle approximation is applicable, the attitude error may also be expressed as a vector resolved about an axis of choice. For example, $\delta\psi_{nb}^n$ is the error in the INS indicated attitude of the body frame with respect to the NED frame, resolved about NED axes. This may be expressed in terms of the coordinate transformation matrix form of the attitude error using [3]

$$[\delta\psi_{nb}^n \wedge] \approx \delta\mathbf{C}_b^n - \mathbf{I}_3. \quad (48)$$

Finally, the specific-force and angular-rate errors from the accelerometer and gyro measurements are

$$\begin{aligned}\delta\mathbf{f}_{ib}^b &= \tilde{\mathbf{f}}_{ib}^b - \mathbf{f}_{ib}^b \\ \delta\boldsymbol{\omega}_{ib}^b &= \tilde{\boldsymbol{\omega}}_{ib}^b - \boldsymbol{\omega}_{ib}^b.\end{aligned}$$

2) Short-Term Straight-Line Error Propagation: As inertial navigation is most commonly integrated with GNSS or other sensors, short-term error propagation is of the most relevance. For the short-term case, the effects of the curvature and rotation of the Earth and the gravity model feedback may be neglected. Here, the simplest case, in which the host vehicle is traveling in a straight line at a constant velocity and remains level, is considered. Consequently, there are no dynamics-induced errors.

Fig. 10 shows the position error growth with constant velocity, acceleration, attitude, and angular-rate errors. The position error is the integral of the velocity error, so with a constant velocity error,

$$\delta\mathbf{r}_{eb}^n(t) = \delta\mathbf{v}_{eb}^n t. \quad (49)$$

Thus, a 0.1-m s⁻¹ initial velocity error produces a 30-m position error after 300 s (5 min).

The velocity error is the integral of the acceleration error, so the velocity and position errors resulting from a constant accelerometer bias are

$$\delta\mathbf{v}_{eb}^n(t) \approx \mathbf{C}_b^n \mathbf{b}_a t, \quad \delta\mathbf{r}_{eb}^n(t) \approx \frac{1}{2} \mathbf{C}_b^n \mathbf{b}_a t^2, \quad (50)$$

and a 0.01-m s⁻² (~1 mg) accelerometer bias produces a 450-m position error after 300 s. Acceleration errors can also result from gravity modeling approximations. For example, the models in Sections IV.C.3 and IV.D are typically accurate to ~10⁻³ m s⁻² (0.1 mg) in each direction [4, 20].

Attitude errors produce errors in the transformation of the specific-force resolving axes from the body frame to the NED frame, resulting in errors in the acceleration resolved in that frame. Fig. 11 illustrates this. Where the attitude error may be expressed as a small angle, the resulting acceleration error is

$$\delta\mathbf{a}_{eb}^n(t) \approx \delta\psi_{nb}^n \wedge (\mathbf{C}_b^n \tilde{\mathbf{f}}_{ib}^b). \quad (51)$$

In the constant-velocity and level example, the specific force comprises only the reaction to gravity. Thus, pitch (body-frame *y*-axis) attitude errors couple into along-track (body-frame *x*-axis) acceleration errors, and roll (body-frame *x*-axis) attitude errors couple into across-track (body-frame *y*-axis) acceleration errors. These acceleration errors are integrated to produce the following velocity and position errors:

$$\delta\mathbf{v}_{eb}^n(t) \approx \delta\psi_{nb}^n \wedge \begin{pmatrix} 0 \\ 0 \\ -g \end{pmatrix} t, \quad \delta\mathbf{r}_{eb}^n(t) \approx \frac{1}{2} \delta\psi_{nb}^n \wedge \begin{pmatrix} 0 \\ 0 \\ -g \end{pmatrix} t^2. \quad (52)$$

A 1-mrad (0.057°) initial attitude error therefore leads to a position error of ~440 m after 300 s. Similarly, the velocity and position errors due to the gyro bias are

$$\delta\mathbf{v}_{eb}^n(t) \approx \frac{1}{2}(\mathbf{C}_b^n \mathbf{b}_g) \wedge \begin{pmatrix} 0 \\ 0 \\ -g \end{pmatrix} t^2, \quad \delta\mathbf{r}_{eb}^n(t) \approx \frac{1}{6}(\mathbf{C}_b^n \mathbf{b}_g) \wedge \begin{pmatrix} 0 \\ 0 \\ -g \end{pmatrix} t^3, \quad (53)$$

while a 10^{-5} -rad s^{-1} (2.1°h^{-1}) gyro bias produces a ~439-m position error after 300 s.

The other major source of error in this scenario is inertial sensor noise, which may be considered white over timescales exceeding 1 s. If the single-sided accelerometer noise PSD is S_a , the standard deviations of the ensuing velocity and position errors are

$$\begin{aligned} \sigma(\delta v_{eb,i}^n) &= \sqrt{S_a t} \quad i \in N, E, D \\ \sigma(\delta r_{eb,i}^n) &= g\sqrt{\frac{1}{3} S_a t^3} \end{aligned} \quad . \quad (54)$$

Similarly, if the gyro noise PSD is S_g , the standard deviations of the ensuing attitude errors and horizontal position and velocity errors are

$$\begin{aligned} \sigma(\delta\psi_{nb,i}^n) &= \sqrt{S_g t} \quad i \in N, E, D \\ \sigma(\delta v_{eb,j}^n) &= g\sqrt{\frac{1}{3} S_g t^3} \quad j \in N, E \\ \sigma(\delta r_{eb,j}^n) &= g\sqrt{\frac{1}{5} S_g t^5} \end{aligned} \quad . \quad (55)$$

Fig. 12 shows the growth in the position error standard deviation because of sensor noise. If the accelerometer random-noise PSD is $10^{-6} \text{ m}^2 \text{ s}^{-3}$ (corresponding to a root PSD of ~100 $\mu\text{g}/\sqrt{\text{Hz}}$), the position error standard deviation after 300 s is 3 m per axis. Similarly, if the gyro random-noise PSD is $10^{-9} \text{ rad}^2 \text{ s}^{-1}$

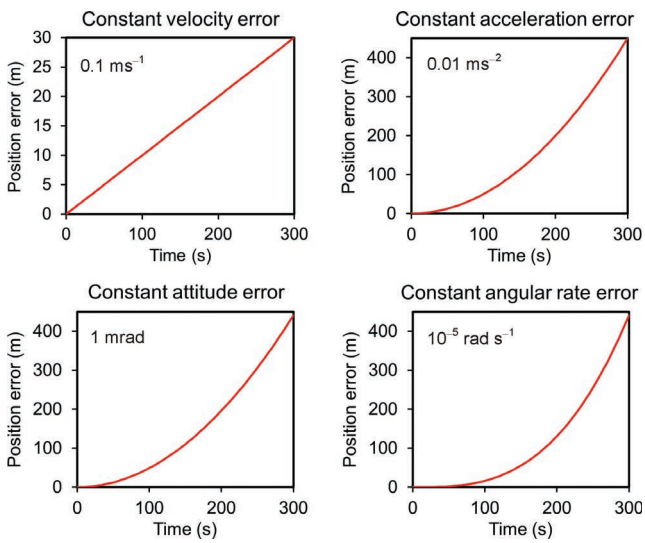


Fig. 10.
Short-term straight-line position error standard deviation growth per axis because of inertial sensor noise. (From [3] © Paul Groves 2013. Reproduced with permission.)

(a root PSD of ~0.1°/ $\sqrt{\text{h}}$), the position error standard deviation after 300 s is ~22 m per horizontal axis.

Fig. 13 shows the growth of the horizontal position error standard deviation using tactical- and aviation-grade INSs with the characteristics listed in Table 2. The tactical-grade INS error is more than an order of magnitude bigger than that of the aviation-grade INS after 300 s. The difference in horizontal and vertical performance of the tactical-grade INS arises because the gyro bias dominates, and under constant velocity conditions, this only affects horizontal navigation. For the aviation-grade INS, the acceleration, roll, and pitch errors dominate. The initial position error has little impact after the first minute. Where a tactical-grade INS is calibrated through sensor integration or fine alignment (Section VI), the errors are reduced by about a factor of 10.

3) Longer Term Error Propagation: Longer term INS error propagation is affected by the gravity model. A horizontal position error results in the gravity model assuming that gravity acts at an angle to its true direction, producing a horizontal acceleration error. However, this acceleration error is in the opposite direction to the position error, providing negative feedback and correcting the error. Consequently, the position error due to a velocity, attitude, or acceleration error undergoes a bounded simple harmonic oscillation, known as a Schuler oscillation, with a period of ~84 min. The position error due to an angular-rate error comprises the sum of a linearly growing term and an oscillatory term. Thus, over the long term, it is the quality of the gyros that determines the overall accuracy of an INS. Further details may be found in [3, 4, 20].

A positive height error causes the magnitude of the gravity to be underestimated, resulting in a positive vertical acceleration error. Thus, in the vertical direction, there is positive feedback through the gravity model and the solution is unstable.

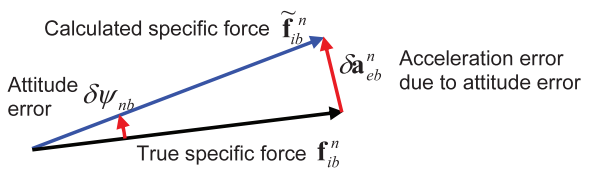


Fig. 11.
Acceleration error due to attitude error. (From [3] © Paul Groves 2013. Reproduced with permission.)

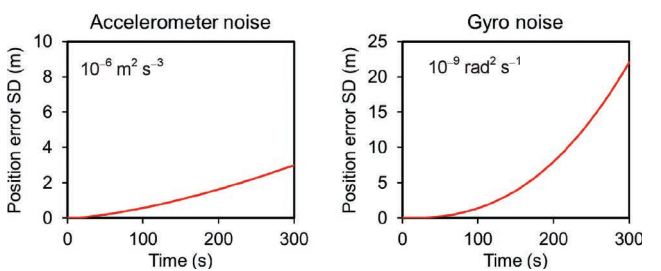


Fig. 12.
Short-term straight-line position error standard deviation growth per axis because of inertial sensor noise. (From [3] © Paul Groves 2013. Reproduced with permission.)

Table 2..

Sensor grade	Tactical	Aviation
Initial position error SD	10 m	10 m
Initial velocity error SD	0.1 m s ⁻¹	0.01 m s ⁻¹
Initial (roll and pitch) attitude error SD	1 mrad	0.1 mrad
Accelerometer bias SD	0.01 m s ⁻² (1 mg)	0.001 m s ⁻² (0.1 mg)
Gyro bias SD	5×10 ⁻⁵ rad s ⁻¹ (10° h ⁻¹)	5×10 ⁻⁸ rad s ⁻¹ (0.01° h ⁻¹)
Accelerometer noise PSD	10 ⁻⁶ m ² s ⁻³ (100°g/√Hz) ²	10 ⁻⁷ m ² s ⁻³ (32°g/√Hz) ²
Gyro noise PSD	10 ⁻⁹ rad ² s ⁻¹ (0.1°/√h) ²	10 ⁻¹² rad ² s ⁻¹ (0.003°/√h) ²

SD = standard deviation.

Historically, aircraft INSs have been integrated with barometric altimeters to stabilize the vertical channel. Today, this stabilization may also be achieved through integration with GNSS. For land and sea applications, a motion constraint may be used.

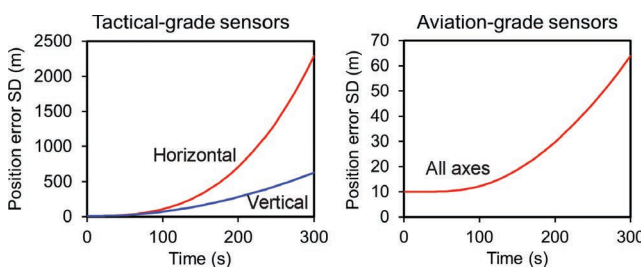
4) *Maneuver-Dependent Errors:* Much of the error propagation in inertial navigation depends on the host-vehicle maneuvers. As explained in Section IV.E.2, the effect of attitude errors on the velocity and position solutions depends on the specific force. The heading error only has an impact during maneuvers. A linear acceleration or deceleration maneuver couples the heading error into the cross-track velocity and the pitch error into the vertical velocity. A turn produces transverse acceleration, which couples the heading error into the along-track velocity and the roll error into the vertical velocity.

The heading error is typically an order of magnitude larger than the roll and pitch errors because it is more difficult to initialize and calibrate. Consequently, significant maneuvers can lead to rapid changes in velocity error. Fig. 14 shows the velocity errors of an aircraft, initially flying north at 100 m s⁻¹ with north and east velocity errors of 0.05 m s⁻¹ and 0.1 m s⁻¹, respectively, and a heading error of 1 mrad. The aircraft then

accelerates to 200 m s⁻¹, resulting in the east velocity error doubling to 0.2 m s⁻¹. Later, it undergoes a 90° turn to the west at constant speed, which increases the north velocity error to 0.25 m s⁻¹ and drops the east velocity error to zero.

The effect of scale-factor and cross-coupling errors, gyro g-dependent errors, and higher order inertial sensor errors on navigation error growth also depends on the maneuvers. In the previous example, a 500-ppm *x*-accelerometer scale-factor error would produce an increase in north velocity error during the acceleration maneuver of 0.05 m s⁻¹, while a *z*-gyro scale-factor error of -637 ppm would double the heading error to 2 mrad during the turn.

Velocity and direction changes often cancel out over successive maneuvers, so the effects of the scale-factor and cross-coupling errors largely average out. An exception is circular and oval trajectories where the gyro scale-factor and cross-coupling errors produce attitude errors that grow with time. Using tactical-grade gyros with scale-factor and cross-coupling errors of ~300 ppm, the attitude errors will increase by ~0.1° per axis for each circuit completed by the host vehicle. With a circling period of 2 min, the position error will increase by ~400 m per hour.

**Fig. 13.**

Short-term straight-line position error standard deviation growth per axis for tactical- and aviation-grade INSs. (From [3] © Paul Groves 2013. Reproduced with permission.)

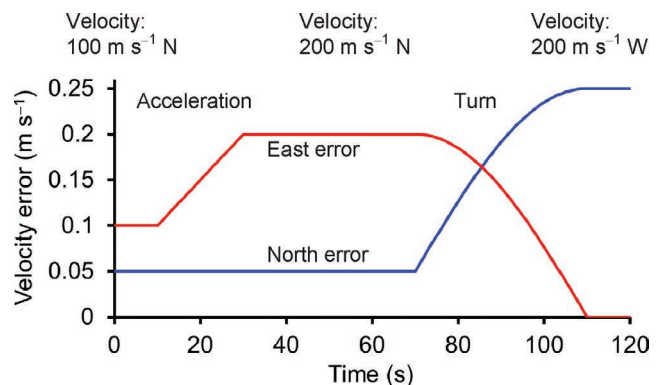
**Fig. 14.**

Illustration of effect of maneuver on velocity error with 1 mrad heading error. (From [3] © Paul Groves 2013. Reproduced with permission.)

With a figure-of-eight trajectory, the attitude error due to gyro scale-factor and cross-coupling errors will be oscillatory and correlated with the direction of travel. This produces a velocity error that increases with each circuit. Using tactical-grade gyros, position errors of several kilometers can build up over an hour.

INS error propagation is also affected by vibration. Synchronized angular oscillation about two orthogonal axes, known as coning, results in a constant angular-rate error. Similarly, linear oscillation synchronized with angular oscillation about an orthogonal axis, known as sculling, results in a constant acceleration error. These coning and sculling errors are larger when the update interval is larger, there are approximations in the navigation equations, or both occur [3, 4].

5) *Indexed IMUs:* In an indexed or carousing IMU, the inertial sensor assembly is regularly rotated with respect to the casing, usually in increments of 90°. This enables the cancellation over time of the position and velocity errors due to the accelerometer and gyro biases. From (50) and (53), the growth in the position and velocity errors depends on the attitude. Therefore, if the direction of an inertial sensor's sensitive axis is regularly reversed, its bias will lead to oscillatory position and velocity errors instead of continuously growing errors. To achieve this, it is rather more convenient to turn the inertial sensor assembly than to turn the entire host vehicle.

Single-axis indexing normally employs rotation of the inertial sensor assembly about the z axis, generally the vertical. This enables cancellation of the effects of x - and y -axis accelerometer and gyro biases but not the effects of the z -axis biases. The z -axis gyro bias has less impact on navigation accuracy, because maneuvers are needed to couple the heading error into the position and velocity errors, while the z -axis accelerometer bias mainly affects vertical positioning, which always requires aid from another sensor or a motion constraint. Dual-axis indexing enables cancellation of the effects of all six sensor biases on horizontal positioning [24]. These systems are designed so that the errors induced by the sensor rotations cancel out over the course of a rotation cycle.

V. ATTITUDE DETERMINATION

This section describes how inertial sensors may be used for absolute attitude determination, both on their own and with magnetometers. Accelerometer leveling, gyrocompassing, magnetic heading determination, and the attitude and heading reference system (AHRS) are described in turn.

A. ACCELEROMETER LEVELING

When an INS is stationary, the only specific force sensed by the accelerometers is the reaction to gravity. The specific-force measurements are resolved along body-frame axes, whereas predictions from a gravity model are resolved along NED. Therefore, from (2) and (11), the attitude, \mathbf{C}_b^n , can be estimated by solving

$$\mathbf{f}_{ib}^b = -\mathbf{C}_n^b \mathbf{g}_b^n(L_b, h_b), \quad (56)$$

given that $\mathbf{a}_{eb}^n = 0$. At the Earth's surface, the reaction to gravity is in the up direction of a local navigation frame. Therefore, neglecting the first two components of \mathbf{g}_b^n and replacing the third column of \mathbf{C}_n^b with the corresponding Euler angles, obtained from (34), gives

$$\begin{pmatrix} f_{ib,x}^b \\ f_{ib,y}^b \\ f_{ib,z}^b \end{pmatrix} = \begin{pmatrix} \sin \theta_{nb} \\ -\cos \theta_{nb} \sin \phi_{nb} \\ -\cos \theta_{nb} \cos \phi_{nb} \end{pmatrix} g_{b,D}^n(L_b, h_b), \quad (57)$$

where θ_{nb} is pitch, ϕ_{nb} is roll, and $g_{b,D}^n$ is the down component of the acceleration due to gravity. This solution is overdetermined. Therefore, gravity can be eliminated to give

$$\theta_{nb} = \arctan \left(\frac{f_{ib,x}^b}{\sqrt{f_{ib,y}^b{}^2 + f_{ib,z}^b{}^2}} \right), \quad \phi_{nb} = \arctan_2(-f_{ib,y}^b, -f_{ib,z}^b), \quad (58)$$

although a four-quadrant arctangent function must be used for roll. Heading cannot be determined by leveling because the orientation of the gravity vector within the body frame is independent of it.

Where the INS is absolutely stationary, the accuracy is determined only by the accelerometer errors. For example, a 1-mrad roll and pitch accuracy is obtained from accelerometers accurate to $10^{-3}g$. Disturbing motion, such as mechanical vibration, wind effects, and human activity, disrupts the leveling process. However, if the motion averages out over time, its effects may be mitigated simply by time averaging the accelerometer measurements over a few seconds.

Leveling should not be performed when the host vehicle is maneuvering, and attempting to do so can lead to large errors. Therefore, accelerometer leveling measurements should only be accepted when $|\mathbf{f}_{ib}^b| \approx |\mathbf{g}_b^n|$.

B. GYROCOMPASSING

When the INS is stationary, the only rotation it senses is that of the Earth, which is about the z direction of an ECEF frame. Measuring this rotation in the body frame enables the heading to be determined, except close to the poles, where the rotation axis and gravity vector coincide. There are two types of gyrocompassing: direct and indirect.

Direct gyrocompassing measures the Earth rotation directly using the gyros. The attitude, \mathbf{C}_b^n , may be obtained by solving

$$\boldsymbol{\omega}_{ib}^b = \mathbf{C}_n^b \mathbf{C}_e^n(L_b, \lambda_b) \begin{pmatrix} 0 \\ 0 \\ \omega_{ie} \end{pmatrix}, \quad (59)$$

given that $\boldsymbol{\omega}_{eb}^n = 0$. Substituting in (31) and rearranging,

$$\begin{pmatrix} \cos L_b \omega_{ie} \\ 0 \\ -\sin L_b \omega_{ie} \end{pmatrix} = \mathbf{C}_b^n \boldsymbol{\omega}_{ib}^b. \quad (60)$$

Solving the middle row of (60), substituting the corresponding Euler angles into C_{ib}^n , enables the heading to be determined without knowledge of position, provided the roll and pitch are known (e.g., from leveling):

$$\begin{aligned}\psi_{nb} &= \arctan_2(\sin\psi_{nb}, \cos\psi_{nb}) \\ \sin\psi_{nb} &= -\omega_{ib,y}^b \cos\phi_{nb} + \omega_{ib,z}^b \sin\phi_{nb} \\ \cos\psi_{nb} &= \omega_{ib,x}^b \cos\theta_{nb} + \omega_{ib,y}^b \sin\phi_{nb} \sin\theta_{nb} + \omega_{ib,z}^b \cos\phi_{nb} \sin\theta_{nb}\end{aligned}. \quad (61)$$

Again, a four-quadrant arctangent function must be used. Levelling and direct gyrocompassing may also be performed in one step where the latitude is known [4].

If there is disturbing motion, the gyro measurements must be time averaged. However, even small levels of angular vibration will be much larger than the Earth rotation rate. Therefore, if the INS is mounted on any kind of vehicle, an averaging time of many hours can be required. Consequently, the application of direct gyrocompassing is limited.

Indirect gyrocompassing uses the gyros to compute a relative attitude solution, which is used to transform the specific-force measurements into inertial resolving axes. The direction of the Earth's rotation is then obtained from rotation of the inertially resolved gravity vector about this axis, as shown in Fig. 15. Indirect gyrocompassing typically takes 2 to 10 min, depending on the amount of vibration and disturbance and the accuracy required. Suitable quasistationary alignment algorithms are described in [3, 18, 25].

The accuracy achievable using gyrocompassing depends on gyro performance. Given that $\omega_{ie} \approx 7 \times 10^{-5}$ rad s⁻¹, to obtain a 1-mrad heading initialization at the equator, the gyros must be accurate to $\sim 7 \times 10^{-8}$ rad s⁻¹ (0.01° h⁻¹). Only aviation- and marine-grade gyros are this accurate.

C. MAGNETIC HEADING

A three-axis magnetic compass measures the magnitude and direction of the Earth's magnetic field using a triad of magnetometers with mutually perpendicular sensitive axes. Fluxgate magnetometers, magnetoinductive sensors, and magnetoresistive sensors are all suitable [26]. Accelerometer leveling or an inertial attitude solution is used to determine the pitch and roll. This enables the heading of the unit with respect to the direction of the Earth's magnetic field, known as magnetic north, to be determined using

$$\tilde{\psi}_{mb} = \arctan_2 \left(\frac{-\tilde{m}_{m,y}^b \cos\hat{\phi}_{nb} + \tilde{m}_{m,z}^b \sin\hat{\phi}_{nb}}{\tilde{m}_{m,x}^b \cos\hat{\theta}_{nb} + \tilde{m}_{m,y}^b \sin\hat{\phi}_{nb} \sin\hat{\theta}_{nb} + \tilde{m}_{m,z}^b \cos\hat{\phi}_{nb} \sin\hat{\theta}_{nb}} \right), \quad (62)$$

where \tilde{m}_m^b is the measured magnetic flux density and a four-quadrant arctangent function must be used.

The heading with respect to true north is then given by

$$\psi_{nb} = \tilde{\psi}_{mb} + \alpha_{nE}, \quad (63)$$

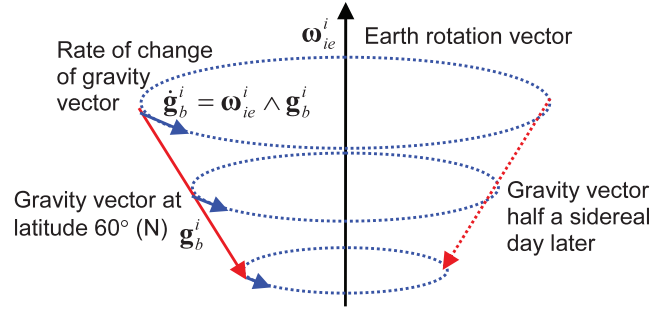


Fig. 15.

Earth rotation and gravity vectors resolved in ECI-frame axes. (From [3] © Paul Groves 2013. Reproduced with permission.)

where α_{nE} is the declination angle or magnetic variation of the Earth's magnetic field. This is the bearing of the magnetic field from true north, and it varies predictably with both position and time. Global models, such as the International Geomagnetic Reference Field and the U.S./U.K. World Magnetic Model, are updated every 5 years. They are typically accurate to $\sim 0.5^\circ$ but can exhibit errors of several degrees in places [26]. Higher resolution national models are available for some countries.

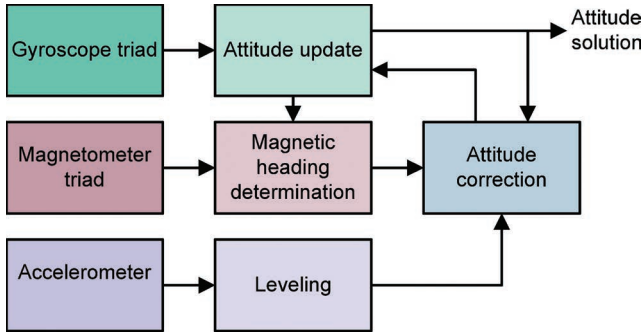
Further errors arise because of magnetic fields from other sources. Land applications are affected by man-made objects, such as vehicles, buildings, bridges, lamp posts, and power lines [27, 28]. These fields can be significant several meters away and cannot easily be distinguished from the Earth's magnetic field. These local anomalies may be detected by comparing the magnitude of the measured magnetic flux density with that of the Earth's magnetic field, enabling inconsistent measurements to be rejected. This may be enhanced by also comparing orientation of the magnetic field with respect to the vertical [29]. However, heading errors of several degrees can remain undetected, while out-of-date heading measurements must be used when an anomaly is detected. Better performance is thus obtained if the magnetic heading is also smoothed using another sensor, such as gyros.

In addition to the geomagnetic field and local anomalies, the magnetometers measure the magnetic field of the navigation system, the host vehicle, and any equipment carried. This comprises a mixture of hard-iron and soft-iron magnetism. Hard-iron magnetism is simply the magnetic fields produced by permanent magnets and electrical equipment. It is usually a few percent of the Earth's magnetic field but can sometimes exceed it. Soft-iron magnetism is produced by materials that distort the underlying magnetic field. It is typically largest in ships, where it can distort the magnetic field by $\sim 10\%$.

As the equipment magnetism moves with the magnetic compass, it can be calibrated using a process known as swinging, whereby a series of measurements are taken with the instrument at different orientations at a fixed location, varying the roll and pitch, as well as the heading [30, 31].

D. ATTITUDE AND HEADING REFERENCE SYSTEM

Fig. 16 depicts an AHRS, which comprises a low-cost IMU with consumer- or tactical-grade sensors and a magnetic com-

**Fig. 16.**

Basic schematic of an AHRS. (From [3] © Paul Groves 2013. Reproduced with permission.)

pass. It is typically used for low-cost aviation applications [32], such as private aircraft and UAVs, and provides a three-component inertial attitude solution without position and velocity. For marine applications, it is sometimes known as a strapdown gyrocompass.

The attitude is maintained by integrating the gyro measurements. The accelerometers measure roll and pitch by leveling (Section V.A), which is used to correct the gyro-derived pitch. Similarly, the magnetic compass (Section V.C) is used to correct the gyro-derived heading. This may be accomplished using a simple smoothing filter:

$$\begin{aligned}\hat{\phi}_{nb}(t) &= W_l \hat{\phi}_{nb,l}(t) + (1 - W_l)[\hat{\phi}_{nb}(t - \tau) + \dot{\phi}_{nb}\tau] \\ \hat{\theta}_{nb}(t) &= W_l \hat{\theta}_{nb,l}(t) + (1 - W_l)[\hat{\theta}_{nb}(t - \tau) + \dot{\theta}_{nb}\tau] \\ \hat{\psi}_{nb}(t) &= W_m \hat{\psi}_{nb,m}(t) + (1 - W_m)[\hat{\psi}_{nb}(t - \tau) + \dot{\psi}_{nb}\tau]\end{aligned}, \quad (64)$$

where t is time; τ is the time interval; $\hat{\phi}_{nb}$, $\hat{\theta}_{nb}$, and $\hat{\psi}_{nb}$ are the roll, pitch, and yaw solutions, respectively; $\hat{\phi}_{nb,l}$ and $\hat{\theta}_{nb,l}$ are the roll and pitch measurements from leveling, respectively; $\hat{\psi}_{nb,m}$ is the heading obtained from the magnetic compass; W_l is the leveling weighting; W_m is the magnetometer weighting; and $\dot{\phi}_{nb}$, $\dot{\theta}_{nb}$, and $\dot{\psi}_{nb}$ are the roll rate, pitch rate, and yaw rate, respectively, derived from the gyro measurements using

$$\begin{pmatrix} \dot{\phi}_{nb} \\ \dot{\theta}_{nb} \\ \dot{\psi}_{nb} \end{pmatrix} \approx \begin{pmatrix} 1 & \sin \hat{\phi}_{nb} \tan \hat{\theta}_{nb} & \cos \hat{\phi}_{nb} \tan \hat{\theta}_{nb} \\ 0 & \cos \hat{\phi}_{nb} & -\sin \hat{\phi}_{nb} \\ 0 & \sin \hat{\phi}_{nb} / \cos \hat{\theta}_{nb} & \cos \hat{\phi}_{nb} / \cos \hat{\theta}_{nb} \end{pmatrix} \mathbf{o}_{ib}^b. \quad (65)$$

The Earth rotation and transport rate (Section IV.D) must be neglected where position and velocity are unknown.

More sophisticated AHRSs use a Kalman filter (Section VI) to perform the attitude integration. In either case, the weighting of the leveling measurements is normally reduced or zeroed when host-vehicle maneuvers are detected. Similarly, the magnetic heading measurements may be down-weighted or rejected when magnetic anomalies are detected.

Performance depends on the quality of the inertial sensors and the type of processing used. A typical AHRS provides roll and pitch to a 10-mrad (0.6°) accuracy and heading to a 20-mrad (1.2°) accuracy, but this may be degraded by a factor of 2 during high-dynamic maneuvers.

VI. INTEGRATION AND ALIGNMENT

As explained in Section IV.E, the error in the position, velocity, and attitude solution of an INS normally grows with time, primarily because of IMU measurement errors but also because of initialization errors and approximations in the navigation equations. This error growth may be minimized by using a series of position- or velocity-aiding measurements, or both, from another source. This is known as integration where the measurements are provided continually and alignment where they are only available during the initialization process. In some systems, attitude measurements are also provided. However, where there is sufficient maneuvering, the attitude errors may be inferred from position and velocity measurements. The inertial sensor errors may also be calibrated.

Inertial navigation may be integrated with many navigation technologies [3, 19]. INS is most commonly integrated with GNSSs, such as a GPS. A GNSS computes a position solution from measurements of the time taken for radio signals to propagate from a constellation of orbiting satellites [33, 34]. Unlike an INS, the GNSS position solution does not normally degrade with time.

For indoor navigation, inertial navigation may be integrated with positioning systems using other radio signals, such as Wi-Fi and ultra-wideband, while for underwater applications, acoustic ranging is typically used. Position information may also be inferred from cameras, laser scanners, radar, and sonar. For land applications, position corrections may be obtained from map matching on the basis that road vehicles normally travel on roads, trains stay on tracks, and pedestrians don't walk through walls. In multisensor integrated navigation systems, a variety of navigation and positioning technologies are combined [3, 19]. This may include additional dead-reckoning technologies, such as odometry (wheel speed), Doppler radar, or Doppler sonar. Sources of attitude information include magnetometers (Section V.C), cameras, and multiantenna GNSS.

An important question is why inertial navigation is used when a drift-free position and velocity solution is available from another source. There are several reasons. First, an INS typically exhibits less short-term noise than technologies, such as GNSS, that measure position directly, so the integrated solution is smoother and more accurate. Second, an INS provides a much higher bandwidth, with an update rate of at least 50 Hz and lower latency than many other sensors. Third, attitude, acceleration, and angular rate are provided, in addition to position and velocity. Finally, INS integration enables a continuous navigation solution to be maintained, whereas position-fixing technologies fail when insufficient signals are received or landmarks are observed. For example, GNSS signals are highly vulnerable to incidental and deliberate interference, and they can be blocked by buildings and mountainous terrain.

Alignment algorithms may use the same sources of aiding measurements as integration algorithms. In addition, transfer alignment uses velocity, and sometimes attitude, measurements from another INS or integrated INS/GNSS aboard the same host vehicle, while quasistationary alignment derives aiding

measurements from knowledge that the INS is approximately stationary with respect to the Earth [3, 18, 25].

Fig. 17 shows the basic configuration of a typical integrated navigation system. The integration algorithm, usually based on a Kalman filter, compares the INS with the outputs of an aiding system, such as GNSS, and estimates corrections to the inertial position, velocity, and attitude solution, usually alongside other parameters. The corrected INS then forms the integrated navigation solution, and the closed-loop correction is shown in Fig. 17. This architecture ensures that an integrated navigation solution is always produced, regardless of the availability of aiding measurements. A detailed discussion of integration architectures may be found in [3]. Fig. 18 shows the typical stages of an integration or alignment algorithm.

The rest of this section comprises an introduction to the Kalman filter; a discussion of state selection, system propagation, and measurement update; and the correction of the navigation solution.

A. INTRODUCTION TO THE KALMAN FILTER

The Kalman filter is an estimation algorithm that maintains real-time estimates of a number of parameters of a system, such as its position and velocity, which may continually change. The estimates are updated using a stream of measurements that are subject to noise. The measurements must be functions of the parameters estimated, but the set of measurements at a given time need not contain sufficient information to uniquely determine the values of the parameters at that time.

The Kalman filter uses knowledge of the deterministic and statistical properties of the system parameters and the measurements to obtain optimal estimates given the information available. It is a Bayesian estimation technique. It is supplied with an initial set of estimates and then operates recursively, updating its working estimates as a weighted average of their previous values and new values derived from the latest measurement data.

A Kalman filter has five core elements: the state vector and covariance, the system model, the measurement vector and covariance, the measurement model, and the algorithm.

The state vector, \mathbf{x} , is the set of parameters describing a system, known as states, which the Kalman filter estimates. For integration and alignment of INSs, the states include the position error, velocity error, and attitude error. Associated with the state vector is an error covariance matrix, \mathbf{P} . This represents the uncertainties in the Kalman filter's state estimates and the degree of correlation between the errors in those estimates. This correlation information may be used to infer one state from another. Thus, the velocity error could be estimated from the rate of change of the position error. Similarly, the attitude and acceleration errors may be inferred from the variation of the velocity error.

The system model, also known as the process model or time-propagation model, describes the known variation of the Kalman filter states over time. For example, the position error varies with time as the integral of the velocity error. This is expressed using the transition matrix, Φ , which relates the value of the state vector at the previous epoch in time to its current value. The transition matrix is also used to update the state

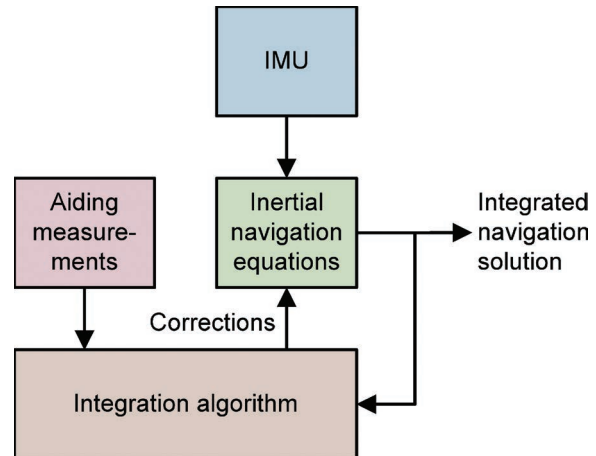


Fig. 17.
Generic integration architecture [3].

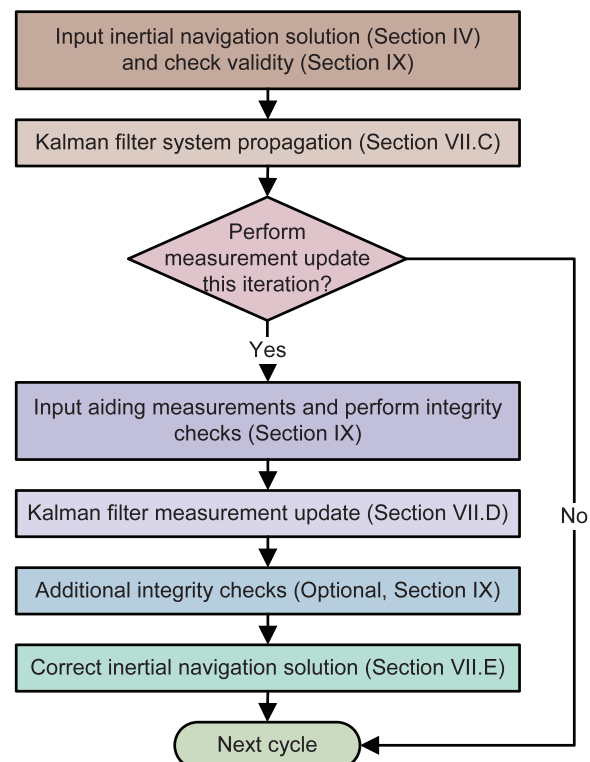


Fig. 18.
Typical stages of an integration or alignment algorithm [3].

error covariance matrix. However, the state uncertainties must also be increased with time to account for unknown changes in the system, such as random noise on an instrument output. This variation in the true values of the states is known as system noise or process noise and is described by the system noise covariance matrix, \mathbf{Q} .

The measurement vector, \mathbf{z} , is a set of simultaneous measurements of properties of the system that are functions of the state vector, such as the difference in navigation solution between an INS under calibration and a reference navigation sys-

tem. This is the information from which all state estimates are derived after initialization. Associated with the measurement vector is a measurement noise covariance matrix, \mathbf{R} , which describes the statistics of the noise on the measurements.

The measurement model describes how the measurements vary as a function of the states. For example, the difference in velocity measurements between an INS and a reference system is directly proportional to the INS velocity error. In a linear Kalman filter, the measurement model is

$$\mathbf{z} = \mathbf{Hx} + \mathbf{w}_m, \quad (66)$$

where \mathbf{H} is the measurement matrix and \mathbf{w}_m is the measurement noise vector. The measurement model also enables the Kalman filter to compare the measurement noise covariance, \mathbf{R} , with the state error covariance, \mathbf{P} , to determine the optimal weighting of the new measurements.

The Kalman filter algorithm uses the measurement vector, measurement model, and system model to maintain optimal estimates of the state vector. It consists of two phases, system propagation and measurement update, which together comprise up to 10 steps per iteration. These are shown in Fig. 19. Steps 1–4 form the system-propagation phase, and steps 5–10 form the measurement-update phase. Clear introductions to Kalman filter-based estimation, suitable for beginners, may be found in [35, 36], while more comprehensive coverage is presented in [37, 38] and its application to integrated navigation is described in detail in [3, 10, 19]. Here, a relatively simple example is presented.

B. STATE SELECTION

Most INS integration and alignment algorithms implement an error-state Kalman filter (or derivative thereof), where the states estimated comprise a selection of the INS errors, defined in Section IV.E.1. The position and velocity errors are always estimated. For all but the highest grades of INS, there is significant benefit in estimating the attitude error, which is expressed here in the small angle form.

The choice of inertial instrument errors (Section III) to estimate depends on how they affect the position, velocity, and attitude solution. If an IMU error has a significant impact on the navigation accuracy, it will be observable. Conversely, if its impact is much less than that of the random noise, which cannot be calibrated, it will not be observable. In practice, this depends on the user dynamics and the IMU design.

The following discussion assumes that position, velocity, or both types of measurements are available from an aiding source but that attitude measurements are not. The attitude errors are therefore observed through the variation in the velocity error they produce.

Except where they are very small, the accelerometer biases should always be estimated where the attitude errors are estimated. Conversely, the attitude errors should always be estimated where the accelerometer biases are estimated. Otherwise, the attitude error estimates are contaminated by the effects of the acceleration errors, or vice versa. This is because both types

of error lead to a linear growth in velocity error and quadratic growth in position error (Section IV.E).

As (51) shows, acceleration errors arise where the specific force is perpendicular to the rotation axis of the attitude error. Thus, the heading error only produces a velocity error when there is acceleration in the horizontal plane. Therefore, the navigation system's host must undergo significant maneuvering for the INS heading error to be observed and calibrated. When the navigation system is level and not accelerating, the vertical accelerometer bias is the only Kalman filter state that causes growth of the vertical velocity error. This makes it the most observable of the accelerometer biases, so vertical navigation is normally better than horizontal during periods of a few minutes without aiding measurements. The roll and pitch attitude errors and horizontal accelerometer biases are observed as linear combinations under conditions of constant acceleration and attitude. To fully separate the estimates of these states, the host vehicle must turn, which a period of forward acceleration enables separation of the pitch error and forward accelerometer bias.

The gyro biases are also estimated in most integration and alignment algorithms. These are the only significant error sources that produce a quadratic growth in the velocity error with time.

Whether it is worth estimating the accelerometer and gyro scale-factor and cross-coupling errors or the gyro g -dependent biases depends on the size of the errors and the behavior of the host vehicle (Section IV.E.3). These errors have the most impact in highly dynamic applications, such as motor sports, combat aircraft, and some guided weapons. Gyro scale-factor and cross-coupling errors can also be significant for aircraft performing circling movements and roll-stabilized guided weapons. A common mistake is to estimate scale-factor errors but not cross-coupling errors, because they are usually of a similar magnitude. For very high-precision applications, gravity modeling errors may be estimated.

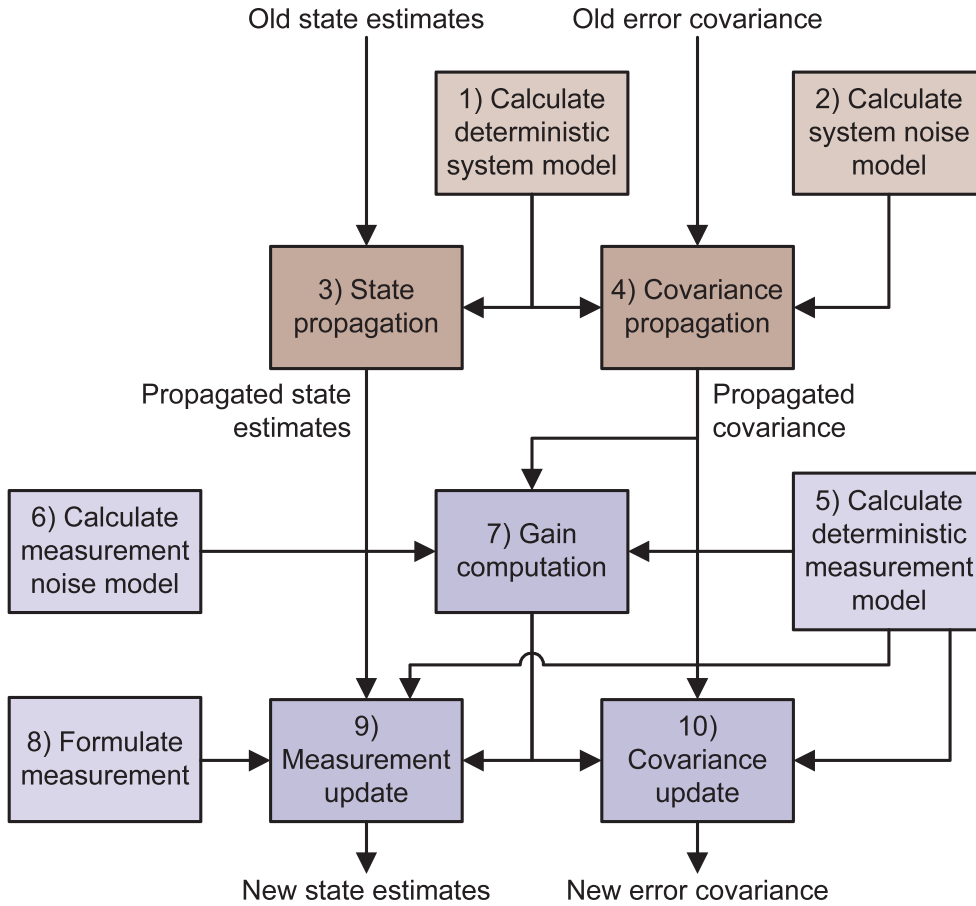
The Kalman filter may also estimate errors exhibited by other components of an integrated navigation system, such as GNSS clock errors [3, 19, 36]. However, this is outside the scope of this article.

For the integration and alignment algorithm described in the following subsections, the INS attitude and velocity errors, resolved in NED axes; the position error expressed in terms of latitude, longitude, and height; and the accelerometer and gyro biases are estimated. The state vector is thus

$$\mathbf{x} = \begin{pmatrix} \delta\Psi_{nb}^n \\ \delta\mathbf{v}_{eb}^n \\ \delta\mathbf{p}_b \\ \mathbf{b}_a \\ \mathbf{b}_g \end{pmatrix}, \quad \delta\mathbf{p}_b = \begin{pmatrix} \delta L_b \\ \delta\lambda_b \\ \delta h_b \end{pmatrix}. \quad (67)$$

C. SYSTEM PROPAGATION

The system model is used to propagate forward the Kalman filter state estimates and their associated error covariance, from one epoch in time to the next. The state estimates are propagated using

**Fig. 19.**

Kalman filter algorithm steps. (From [3] © Paul Groves 2013. Reproduced with permission.)

$$\hat{\mathbf{x}}_k^- = \Phi_{k-1} \hat{\mathbf{x}}_{k-1}^+, \quad (68)$$

where $\hat{\mathbf{x}}_k^-$ is the vector of state estimates at epoch k before the incorporation of measurement information, $\hat{\mathbf{x}}_{k-1}^+$ is the vector of state estimates at epoch $k - 1$ after the measurement update, and Φ_{k-1} is the transition matrix from epoch $k - 1$ to epoch k .

The transition matrix is derived from the dynamic model,

$$\dot{\mathbf{x}}(t) = \mathbf{F}(t)\mathbf{x}(t) + \mathbf{G}(t)\mathbf{w}_s(t), \quad (69)$$

where \mathbf{F} is the system matrix, \mathbf{G} is the system noise distribution matrix, and \mathbf{w}_s is the system noise vector. A key assumption of this model is thus that the time derivative of each state is a linear function of the other states and white Gaussian noise sources. For integration and alignment of most INSs, these assumptions are approximately correct. For short time intervals, the transition matrix may be approximated to [3, 35–38]

$$\Phi_{k-1} \approx \mathbf{I} + \mathbf{F}_{k-1}\tau_s, \quad (70)$$

where τ_s is the time interval between successive epochs.

For INS integration and alignment, much of the system model for the state vector defined in (67) is intuitive. The rate of change of the attitude error is dominated by the gyro bias, the rate of change of the velocity error is dominated by the accelerometer bias, and the rate of change of the position error is dominated by the velocity error. However, additional dependencies must be modeled because of the rotation of the NED axes with respect to the Earth as the system moves, the rotation of the Earth with respect to inertial space, and the variation of gravity with height. The derivation of the system model is fully described in [3, 19]. Here, only the result is presented. The system matrix is

$$\mathbf{F} = \begin{pmatrix} \mathbf{F}_{11}^n & \mathbf{F}_{12}^n & \mathbf{F}_{13}^n & \mathbf{0}_3 & \hat{\mathbf{C}}_b^n \\ \mathbf{F}_{21}^n & \mathbf{F}_{22}^n & \mathbf{F}_{23}^n & \hat{\mathbf{C}}_b^n & \mathbf{0}_3 \\ \mathbf{0}_3 & \mathbf{F}_{32}^n & \mathbf{F}_{33}^n & \mathbf{0}_3 & \mathbf{0}_3 \\ \mathbf{0}_3 & \mathbf{0}_3 & \mathbf{0}_3 & \mathbf{0}_3 & \mathbf{0}_3 \\ \mathbf{0}_3 & \mathbf{0}_3 & \mathbf{0}_3 & \mathbf{0}_3 & \mathbf{0}_3 \end{pmatrix}, \quad (71)$$

where

$$\mathbf{F}_{11}^n = -\left[(\hat{\boldsymbol{\omega}}_{ie}^n + \hat{\boldsymbol{\omega}}_{en}^n) \wedge \right] \quad \hat{\boldsymbol{\omega}}_{ie}^n = \omega_{ie} \begin{pmatrix} \cos \hat{L}_b \\ 0 \\ -\sin \hat{L}_b \end{pmatrix}, \quad (72)$$

$$\mathbf{F}_{12}^n = \begin{bmatrix} 0 & \frac{-1}{R_E(\hat{L}_b) + \hat{h}_b} & 0 \\ \frac{1}{R_N(\hat{L}_b) + \hat{h}_b} & 0 & 0 \\ 0 & \frac{\tan \hat{L}_b}{R_E(\hat{L}_b) + \hat{h}_b} & 0 \end{bmatrix}, \quad (73)$$

$$\mathbf{F}_{13}^n = \begin{bmatrix} \omega_{ie} \sin \hat{L}_b & 0 & \frac{\hat{v}_{eb,E}^n}{(R_E(\hat{L}_b) + \hat{h}_b)^2} \\ 0 & 0 & \frac{-\hat{v}_{eb,N}^n}{(R_N(\hat{L}_b) + \hat{h}_b)^2} \\ \omega_{ie} \cos \hat{L}_b + \frac{\hat{v}_{eb,E}^n}{(R_E(\hat{L}_b) + \hat{h}_b) \cos^2 \hat{L}_b} & 0 & \frac{-\hat{v}_{eb,E}^n \tan \hat{L}_b}{(R_E(\hat{L}_b) + \hat{h}_b)^2} \end{bmatrix}, \quad (74)$$

$$\mathbf{F}_{21}^n = -\left[\left(\hat{\mathbf{C}}_b^n \hat{\mathbf{f}}_{ib}^b \right) \wedge \right], \quad (75)$$

$$\mathbf{F}_{22}^n = \begin{bmatrix} \frac{\hat{v}_{eb,D}^n}{R_N(\hat{L}_b) + \hat{h}_b} & \frac{2\hat{v}_{eb,E}^n \tan \hat{L}_b}{R_E(\hat{L}_b) + \hat{h}_b} - 2\omega_{ie} \sin \hat{L}_b & \frac{\hat{v}_{eb,N}^n}{R_N(\hat{L}_b) + \hat{h}_b} \\ \frac{\hat{v}_{eb,E}^n \tan \hat{L}_b}{R_E(\hat{L}_b) + \hat{h}_b} + 2\omega_{ie} \sin \hat{L}_b & \frac{\hat{v}_{eb,N}^n \tan \hat{L}_b + \hat{v}_{eb,D}^n}{R_E(\hat{L}_b) + \hat{h}_b} & \frac{\hat{v}_{eb,E}^n}{R_E(\hat{L}_b) + \hat{h}_b} + 2\omega_{ie} \cos \hat{L}_b \\ -\frac{2\hat{v}_{eb,N}^n}{R_N(\hat{L}_b) + \hat{h}_b} & -\frac{2\hat{v}_{eb,E}^n}{R_E(\hat{L}_b) + \hat{h}_b} - 2\omega_{ie} \cos \hat{L}_b & 0 \end{bmatrix}, \quad (76)$$

$$\mathbf{F}_{23}^n = \begin{bmatrix} -\frac{(\hat{v}_{eb,E}^n)^2 \sec^2 \hat{L}_b}{R_E(\hat{L}_b) + \hat{h}_b} - 2\hat{v}_{eb,E}^n \omega_{ie} \cos \hat{L}_b & 0 & \frac{(\hat{v}_{eb,E}^n)^2 \tan \hat{L}_b}{(R_E(\hat{L}_b) + \hat{h}_b)^2} - \frac{\hat{v}_{eb,N}^n \hat{v}_{eb,D}^n}{(R_N(\hat{L}_b) + \hat{h}_b)^2} \\ \left(\frac{\hat{v}_{eb,N}^n \hat{v}_{eb,E}^n \sec^2 \hat{L}_b}{R_E(\hat{L}_b) + \hat{h}_b} + 2\hat{v}_{eb,N}^n \omega_{ie} \cos \hat{L}_b \right) & 0 & -\frac{\hat{v}_{eb,N}^n \hat{v}_{eb,E}^n \tan \hat{L}_b + \hat{v}_{eb,N}^n \hat{v}_{eb,D}^n}{(R_E(\hat{L}_b) + \hat{h}_b)^2} \\ -2\hat{v}_{eb,D}^n \omega_{ie} \sin \hat{L}_b & 0 & \frac{(\hat{v}_{eb,E}^n)^2}{(R_E(\hat{L}_b) + \hat{h}_b)^2} + \frac{(\hat{v}_{eb,N}^n)^2}{(R_N(\hat{L}_b) + \hat{h}_b)^2} - \frac{2g_0(\hat{L}_b)}{r_{es}^e(\hat{L}_b)} \end{bmatrix}, \quad (77)$$

$$r_{es}^e(\hat{L}_b) = R_E(\hat{L}_b) \sqrt{1 - e(2 - e) \sin^2 \hat{L}_b}, \quad (78)$$

$$\mathbf{F}_{32}^n = \begin{bmatrix} \frac{1}{R_N(\hat{L}_b) + \hat{h}_b} & 0 & 0 \\ 0 & \frac{1}{(R_E(\hat{L}_b) + \hat{h}_b) \cos \hat{L}_b} & 0 \\ 0 & 0 & -1 \end{bmatrix}, \quad (79)$$

$$\mathbf{F}_{33}^n = \begin{bmatrix} 0 & 0 & -\frac{\hat{v}_{eb,N}^n}{(R_N(\hat{L}_b) + \hat{h}_b)^2} \\ \frac{\hat{v}_{eb,E}^n \sin \hat{L}_b}{(R_E(\hat{L}_b) + \hat{h}_b) \cos^2 \hat{L}_b} & 0 & -\frac{\hat{v}_{eb,E}^n}{(R_E(\hat{L}_b) + \hat{h}_b)^2 \cos \hat{L}_b} \\ 0 & 0 & 0 \end{bmatrix}. \quad (80)$$

In each case, the caret denotes the navigation solution corrected using the most recent Kalman filter state estimates, $\hat{\mathbf{x}}_{k-1}^+$, as described in Section VI.E. Here, R_E is given by (29), R_N by (39), and g_0 by (43).

Moving from continuous to discrete time, from (70), the transition matrix may be approximated to

$$\Phi \approx \begin{bmatrix} \mathbf{I}_3 + \mathbf{F}_{11}^n \tau_s & \mathbf{F}_{12}^n \tau_s & \mathbf{F}_{13}^n \tau_s & \mathbf{0}_3 & \hat{\mathbf{C}}_b^n \tau_s \\ \mathbf{F}_{21}^n \tau_s & \mathbf{I}_3 + \mathbf{F}_{22}^n \tau_s & \mathbf{F}_{23}^n \tau_s & \hat{\mathbf{C}}_b^n \tau_s & \mathbf{0}_3 \\ \mathbf{0}_3 & \mathbf{F}_{32}^n \tau_s & \mathbf{I}_3 + \mathbf{F}_{33}^n \tau_s & \mathbf{0}_3 & \mathbf{0}_3 \\ \mathbf{0}_3 & \mathbf{0}_3 & \mathbf{0}_3 & \mathbf{I}_3 & \mathbf{0}_3 \\ \mathbf{0}_3 & \mathbf{0}_3 & \mathbf{0}_3 & \mathbf{0}_3 & \mathbf{I}_3 \end{bmatrix}, \quad (81)$$

which is typically acceptable for propagation intervals of 0.2 s or less.

As the state estimates are propagated forward in time using (68), the associated error covariance matrix is propagated using

$$\mathbf{P}_k^- = \Phi_{k-1} \mathbf{P}_{k-1}^+ \Phi_{k-1}^T + \mathbf{Q}_{k-1}, \quad (82)$$

where \mathbf{P}_k^- is the state error covariance matrix at epoch k before the incorporation of measurement information, \mathbf{P}_{k-1}^+ is the error covariance matrix at epoch $k-1$ after the measurement update, and \mathbf{Q}_{k-1} is the system noise covariance matrix, which defines how the uncertainties of the state estimates increase with time, in this case, because of inertial sensor noise and bias variation.

For short propagation intervals ($\tau_s \leq 0.2$ s), a suitable system noise covariance matrix is

$$\mathbf{Q} \approx \begin{bmatrix} S_{rg} \mathbf{I}_3 & \mathbf{0}_3 & \mathbf{0}_3 & \mathbf{0}_3 & \mathbf{0}_3 \\ \mathbf{0}_3 & S_{ra} \mathbf{I}_3 & \mathbf{0}_3 & \mathbf{0}_3 & \mathbf{0}_3 \\ \mathbf{0}_3 & \mathbf{0}_3 & \mathbf{0}_3 & \mathbf{0}_3 & \mathbf{0}_3 \\ \mathbf{0}_3 & \mathbf{0}_3 & \mathbf{0}_3 & S_{bad} \mathbf{I}_3 & \mathbf{0}_3 \\ \mathbf{0}_3 & \mathbf{0}_3 & \mathbf{0}_3 & \mathbf{0}_3 & S_{bgd} \mathbf{I}_3 \end{bmatrix} \tau_s, \quad (83)$$

where S_{rg} , S_{ra} , S_{bad} , and S_{bgd} are the PSDs of, respectively, the gyro random noise, accelerometer random noise, accelerometer bias variation, and gyro bias variation and it is assumed that all gyros and all accelerometers have equal noise characteristics. Values may be obtained from the inertial sensor manufacturer's specifications or from laboratory tests. However, in practice, some trial and error is often needed to determine the best values, particularly because the system noise covariance must also account for the effects of unestimated systematic errors, such as the scale-factor and cross-coupling errors.

D. MEASUREMENT UPDATE

The measurement update phase of the Kalman filter updates the state estimates using information from the measurements. For the INS integration and alignment example presented here, the measurements comprise position and velocity from an aiding system, such as GNSS. This position-domain integration is sometimes called a loosely coupled architecture and may incorporate attitude measurements where available. In the al-

ternative, tightly coupled architecture, ranging, displacement, bearing and elevation, line fix measurements, or some combination of these is used [3, 19]. Tightly coupled integration offers more flexibility and normally leads to a more accurate and robust navigation solution. However, it can only be implemented when the aiding system outputs the necessary information.

The measurement innovation, $\delta\mathbf{z}^-$, comprises the difference between the true measurement vector, \mathbf{z} , and that estimated from the state vector before the measurement update. Thus, for the example presented here, the measurement innovation is the difference between the position and velocity from the aiding system and the corrected INS position and velocity solution:

$$\delta\mathbf{z}_k^- = \begin{pmatrix} \mathbf{S}_p (\hat{\mathbf{p}}_a - \hat{\mathbf{p}}_b - \hat{\mathbf{T}}_{r(n)}^p \hat{\mathbf{C}}_b^n \mathbf{l}_{ba}^b) \\ \hat{\mathbf{v}}_{ea}^n - \hat{\mathbf{v}}_{eb}^n - \hat{\mathbf{C}}_b^n (\hat{\omega}_{ib}^b \wedge \mathbf{l}_{ba}^b) + \hat{\Omega}_{ie}^n \hat{\mathbf{C}}_b^n \mathbf{l}_{ba}^b \end{pmatrix}, \quad (84)$$

where k is the current epoch; $\hat{\mathbf{p}}_a = (\hat{L}_a \ \hat{\lambda}_a \ \hat{h}_a)^T$ and $\hat{\mathbf{p}}_b = (\hat{L}_b \ \hat{\lambda}_b \ \hat{h}_b)^T$ are, respectively, the aiding system and INS curvilinear position solutions; $\hat{\mathbf{v}}_{ea}^n$ and $\hat{\mathbf{v}}_{eb}^n$ are, respectively, the aiding system and INS velocity solutions; $\hat{\mathbf{C}}_b^n$ is the INS attitude solution; $\hat{\omega}_{ib}^b$ is the INS angular rate; \mathbf{l}_{ba}^b is the lever arm from the INS to the aiding sensor; $\hat{\Omega}_{ie}^n$ is obtained from (37) using the INS latitude solution; $\hat{\mathbf{T}}_{r(n)}^p$ given by

$$\hat{\mathbf{T}}_{r(n)}^p = \frac{\partial \mathbf{p}_b}{\partial \mathbf{r}_{eb}^n} = \begin{pmatrix} \frac{1}{R_N(\hat{L}_b) + \hat{h}_b} & 0 & 0 \\ 0 & \frac{1}{(R_E(\hat{L}_b) + \hat{h}_b) \cos \hat{L}_b} & 0 \\ 0 & 0 & -1 \end{pmatrix}, \quad (85)$$

is used to convert position perturbations from Cartesian to curvilinear; and \mathbf{S}_p is the curvilinear position scaling matrix, given by

$$\mathbf{S}_p = \begin{pmatrix} s_{L\lambda} & 0 & 0 \\ 0 & s_{L\lambda} & 0 \\ 0 & 0 & 1 \end{pmatrix}, \quad (86)$$

where a suitable value for $s_{L\lambda}$ is 10^3 . This prevents numerical problems.

The Kalman filter measurement update is then performed in three steps:

$$\mathbf{K}_k = \mathbf{P}_k^- \mathbf{H}_k^T (\mathbf{H}_k \mathbf{P}_k^- \mathbf{H}_k^T + \mathbf{R}_k)^{-1}, \quad (87)$$

$$\hat{\mathbf{x}}_k^+ = \hat{\mathbf{x}}_k^- + \mathbf{K}_k \delta\mathbf{z}_k^-, \quad (88)$$

$$\mathbf{P}_k^+ = (\mathbf{I} - \mathbf{K}_k \mathbf{H}_k) \mathbf{P}_k^-, \quad (89)$$

where \mathbf{K}_k is the Kalman gain matrix, $(\cdot)^{-1}$ denotes matrix inversion, and the measurement matrix can normally be approximated to

$$\mathbf{H}_k \approx \begin{pmatrix} \mathbf{0}_3 & \mathbf{0}_3 & -\mathbf{S}_p & \mathbf{0}_3 & \mathbf{0}_3 \\ \mathbf{0}_3 & -\mathbf{I}_3 & \mathbf{0}_3 & \mathbf{0}_3 & \mathbf{0}_3 \end{pmatrix}, \quad (90)$$

because the coupling of the attitude errors and gyro biases into the measurements through the lever arm is normally weak.

The diagonal components of the measurement noise covariance matrix, \mathbf{R}_k , are the variances of the noise on each component of the position and velocity solution from the aiding system, such as GNSS. Where known, correlation among the different components should be modeled using the off-diagonal elements of \mathbf{R}_k . Furthermore, where this measurement noise is correlated over time, it is necessary to increase \mathbf{R}_k accordingly, multiplying it by the ratio of the correlation time to the update interval. In practice, some trial and error is needed to determine the best values.

E. NAVIGATION SOLUTION CORRECTION

The final step in each cycle of an integration or alignment algorithm is to correct the position, velocity, and attitude solution using

$$\hat{\mathbf{C}}_b^n (+) = (\mathbf{I}_3 - [\delta\hat{\psi}_{nb}^n \wedge]) \hat{\mathbf{C}}_b^n (-), \quad (91)$$

$$\hat{\mathbf{v}}_{eb}^n (+) = \hat{\mathbf{v}}_{eb}^n (-) - \delta\hat{\mathbf{v}}_{eb}^n, \quad (92)$$

and

$$\begin{aligned} \hat{L}_b (+) &= \hat{L}_b (-) - \delta\hat{L}_b \\ \hat{\lambda}_b (+) &= \hat{\lambda}_b (-) - \delta\hat{\lambda}_b, \\ \hat{h}_b (+) &= \hat{h}_b (-) - \delta\hat{h}_b \end{aligned} \quad (93)$$

where the suffixes $(-)$ and $(+)$ denote before and after the correction, respectively, and the small angle approximation is assumed to be applicable to the attitude error. Following these corrections, the attitude error, velocity error, and position error states of the Kalman filter are zeroed, because the information they contain has been transferred to the navigation solution. However, the error covariance matrix, \mathbf{P} , remains unchanged, because the error in the state estimates has not changed.

The accelerometer and gyro biases estimated by the Kalman filter are also fed back to correct the IMU measurements as they are input to the inertial navigation equations. These corrections are in addition to any that may be applied by the IMU's processor. These accelerometer and gyro corrections must be applied on every iteration of the navigation equations, with feedback from the Kalman filter periodically updating them. Consequently, the accelerometer and gyro bias estimates are commonly stored in the navigation processor, with the Kalman filter estimating the residual errors and feeding back perturbations to the biases stored by the navigation processor. The Kalman filter bias estimates are zeroed each time they are used to estimate the navigation processor's bias estimates.

VII. ZERO UPDATES AND MOTION CONSTRAINTS

Zero updates and motion constraints, also known as nonholonomic constraints, use information about the host vehicle (or

user) motion to correct the INS and calibrate the sensor errors. They may be processed as Kalman filter measurements in the same way as aiding sensor measurements in an integrated navigation system (Section VI) and may share the same Kalman filter. They are particularly useful where GNSS reception is poor. The zero velocity update (ZVU), zero angular-rate update (ZARU), land vehicle motion constraints, and pedestrian motion constraints are described in turn.

A. ZERO VELOCITY UPDATES

ZVUs are useful for any application in which the host vehicle or user is often stationary during navigation, such as land vehicle navigation [39] (without odometry, which provides velocity continuously). For pedestrian navigation with a shoe-mounted IMU, a ZVU may be performed on every step. When combined with a method for reducing heading drift, this enables relatively accurate inertial navigation to be performed with very-low-cost consumer-grade inertial sensors [40–42]. Other applications of ZVUs include robotics, helicopter navigation (during touch-downs), and inertial surveying.

The measurement innovation for a ZVU is simply

$$\delta \mathbf{z}_k^- = -\hat{\mathbf{v}}_{eb,k}^n, \quad (94)$$

and the measurement matrix, assuming the state vector defined by (67), is

$$\mathbf{H}_k = (\mathbf{0}_3 \quad -\mathbf{I}_3 \quad \mathbf{0}_3 \quad \mathbf{0}_3 \quad \mathbf{0}_3). \quad (95)$$

Although ZVUs do not provide absolute position information, the Kalman filter models the correlation between the velocity and the position errors in the off-diagonal elements of the error covariance matrix, \mathbf{P} . This enables a ZVU to correct most of the position drift since the last measurement update, ZVU or otherwise [28].

Measurement noise arises because of vibration and disturbances. Vehicles may be disturbed by wind gusts, other vehicles passing, people moving around inside, loading, and unloading. Similarly, a nominally stationary pedestrian may be moving on the spot. The amount of residual motion during a ZVU will depend on what the stationary-condition detection algorithm allows, so there should be a relationship between the assumed measurement noise covariance and the detection threshold.

For extended stationary periods, e.g., during initialization of an aircraft navigation system, zero position displacement measurements can give better performance. The measurement innovation is

$$\delta \mathbf{z}_k^- = \mathbf{S}_p (\hat{\mathbf{p}}_b(t_0) - \hat{\mathbf{p}}_b(t)), \quad (96)$$

where t_0 is when the system first became stationary or the initialization time, as appropriate, and \mathbf{S}_p is given by (86). The measurement matrix is

$$\mathbf{H}_k = (\mathbf{0}_3 \quad \mathbf{0}_3 \quad -\mathbf{S}_p \quad \mathbf{0}_3 \quad \mathbf{0}_3). \quad (97)$$

ZVUs must only be performed when the navigation system is stationary. For surveying applications, stationarity is typically indicated by the operator. However, for navigation, automated detection is needed. Pedestrians may be assumed to be stationary if the magnitude of the accelerometer measurements is close to the acceleration due to gravity for ~0.5 s for body-mounted sensors and 0.2 s for foot-mounted sensors [28, 42]. This is because most parts of the body are constantly accelerating and decelerating during walking and running. The horizontal velocity solution is typically used to determine when a land vehicle is stationary, with accelerometer or gyro measurements used for confirmation [39, 43].

B. ZERO ANGULAR-RATE UPDATE

A ZARU is useful for low-performance gyros with errors at least as large as the angular disturbances to a stationary vehicle or person. ZARUs and ZVUs are sometimes performed separately and sometimes performed together. For land vehicle applications, a zero angular rate may be assumed whenever the vehicle is stationary. For pedestrian applications, ZARUs should be approached with caution because the residual angular motion of a stationary person's body can be much larger than the gyro errors, while a foot can rotate during the stance phase of walking. An additional test is therefore needed to determine whether a ZARU should be performed.

The measurement innovation for a full-IMU ZARU is

$$\delta \mathbf{z}_k^- = -\hat{\boldsymbol{\omega}}_{ib,k}^b. \quad (98)$$

Assuming the state vector defined by (67), the measurement matrix is simply

$$\mathbf{H}_k = (\mathbf{0}_3 \quad \mathbf{0}_3 \quad \mathbf{0}_3 \quad \mathbf{0}_3 \quad -\mathbf{I}_3). \quad (99)$$

The measurement noise covariance represents the variance of the nominally zero angular rate because of vibration and disturbances. For a stationary land vehicle, there will be less disturbance about the yaw axis than about the roll and pitch axes.

C. LAND VEHICLE MOTION CONSTRAINTS

Normal land vehicle motion is subject to two constraints. The velocity of the vehicle is zero along the rotation axis of any of its wheels and in the direction perpendicular to the road or rail surface [44, 45]. The acceleration is not necessarily zero. This vehicle velocity constraint can be applied as a Kalman filter measurement update with measurement innovation

$$\delta \mathbf{z}_k^- = -\begin{pmatrix} 0 & 1 & 0 \\ 0 & 0 & 1 \end{pmatrix} (\hat{\mathbf{C}}_n^b \hat{\mathbf{v}}_{eb}^n - \hat{\boldsymbol{\omega}}_{ib}^b \wedge \mathbf{l}_{rb}^b), \quad (100)$$

where \mathbf{l}_{rb}^b is the lever arm from the center of the rear axle to the origin of the IMU body frame, resolved along the IMU

axes, which are assumed here to be aligned with the forward, right, and down directions of the vehicle body. Assuming the state vector defined by (67) and neglecting the coupling of the attitude errors and gyro biases into the measurements through the lever arm, the measurement matrix may be approximated to

$$\mathbf{H}_k \approx \begin{pmatrix} \mathbf{0}_{2 \times 3} & -\begin{pmatrix} 0 & 1 & 0 \\ 0 & 0 & 1 \end{pmatrix} \hat{\mathbf{C}}_n^b & \mathbf{0}_{2 \times 3} & \mathbf{0}_{2 \times 3} & \mathbf{0}_{2 \times 3} \end{pmatrix}. \quad (101)$$

This is equivalent to a ZVU applied along only two axes. However, the motion-constraint measurements may be applied continuously. If the IMU is not aligned with the vehicle body, the relative orientation may be estimated by the Kalman filter, as may the lever arm [46, 47].

The measurement noise covariance must account for the differences between the true and the assumed vehicle motion. Causes include sideslip of the wheels, the vehicle's suspension system, and engine vibration [44]. The time correlation of these effects may be significant where the measurement update rate is high.

Sideslip can invalidate the transverse velocity constraint when the vehicle turn rate exceeds ~ 0.05 rad s $^{-1}$. Better performance is therefore obtained if the transverse measurements are omitted whenever the yaw rate exceeds a predefined threshold [48].

D. PEDESTRIAN MOTION CONSTRAINTS

In man-made environments, pedestrians tend to walk in approximately straight lines, particularly where walls and roads are in the way. Therefore, the drift in an INS can be constrained by assuming that a person's heading is constant whenever the change in the INS heading solution over a certain interval is below a certain threshold [49]. Indoors, the floor is usually flat, so a constant-height constraint may be assumed unless steps, an escalator, an elevator, or a ramp are detected [50].

VIII. PDR USING STEP DETECTION

Pedestrian navigation is highly challenging. It must work in urban areas, under tree cover, and indoors, where coverage of GNSS and many other radio navigation systems is poor. Inertial sensors can be used to measure motion. However, for pedestrian use, they must be small and light, consume minimal power, and for most applications, be low cost, requiring MEMS sensors to be used. However, these provide very poor inertial navigation performance when used alone, while the combination of low dynamics and high vibration makes them difficult to calibrate using other positioning systems. One option is to use a shoe-mounted IMU with conventional inertial navigation (Section IV) aided by ZVUs (Section VII.A) every step. However, this is impractical for many applications.

This section describes PDR using step detection, whereby the inertial sensors are used for detecting steps. A step is the movement of one foot with the other remaining stationary, while a stride is the successive movement of both feet. This

gives significantly better performance than conventional inertial navigation for sensors mounted on the user's body or in a handheld device, even with tactical-grade sensors [28].

As shown in Fig. 20, a PDR algorithm comprises three phases: step detection, step length estimation, and navigation-solution update. The step-detection phase identifies that a step has taken place. For body-mounted or device-mounted sensors, the vertical or root sum of squares accelerometer signals exhibit a double-peaked oscillatory pattern. Steps can be detected from the peaks [51] or from the points where the specific force rises above or drops below the acceleration due to gravity [52], with a recognition window used to limit false detections.

The step length varies depending on the individual, the slope and texture of the terrain, whether there are obstacles to be negotiated, and whether an individual is tired, carrying things, and walking alone or with others. Thus, PDR implementations that assume a fixed step length for each user are only accurate to $\sim 10\%$ of distance traveled [53]. However, the step length may be modeled as a function of parameters such as the step frequency, the variance of the accelerometer measurements, the slope of the terrain, and the vertical velocity. One model is [42]:

$$\Delta r_p = c_{p0} + \frac{c_{p1}}{\tau_p} + c_{p2}\sigma_f^2 + c_{p3}\hat{\theta}_{nb}, \quad (102)$$

where Δr_p is the PDR-estimated step length, τ_p is the interval between successive steps, σ_f^2 is the variance of the specific-force measurements, $\hat{\theta}_{nb}$ is the estimated angle of the slope, and c_{p0} , c_{p1} , c_{p2} , and c_{p3} are the model coefficients. Using this approach, an accuracy of $\sim 3\%$ of distance traveled may be obtained [54, 55]. The model coefficients for each user may be estimated using measurements from GNSS or another positioning system.

How inertial sensors respond to pedestrian motion depends on their location. Thus, an algorithm optimized for waist-mounted sensors may not give the best results for sensors located in a pocket, in a backpack, or in a device held by the user. Similarly, step-length model coefficients optimized for walking will not give good results for running, turning, and climbing stairs or steps. A robust implementation of PDR should thus incorporate a real-time classification system that

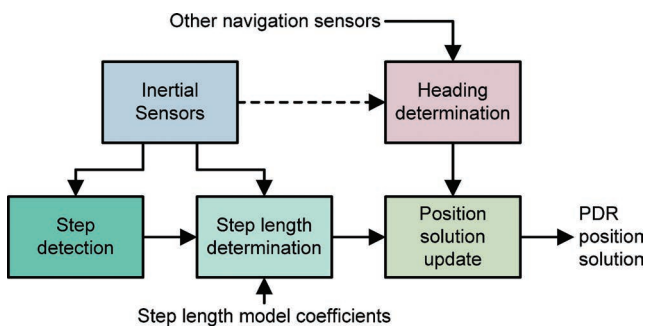


Fig. 20.

PDR processing. (From [3] © Paul Groves 2013. Reproduced with permission.)

detects both the motion type and the sensor location and tunes both the step-detection and the step-length-estimation algorithms accordingly [56, 57].

IX. FAULT DETECTION

There are a number of ways in which an INS can fail. Faults can arise in individual inertial sensors. All inertial sensors can exhibit large errors when the vibration levels are much higher than the system is designed for or there is a mounting failure. The whole IMU or INS may also exhibit a power failure, software failure, or communications failure, which can sometimes be fixed by performing a reset.

To avoid producing a false navigation solution, fault detection is required. The simplest approach is range checks, which may be applied to both the sensor measurements and the navigation solution. Faulty sensors may output measurements outside the operational range specified by the manufacturer or the operating range of the sensor environment. A faulty sensor can also produce a succession of repeated measurements, null measurements, or no measurements.

A fault may also be indicated by a navigation solution outside the operational envelope of the application. Every vehicle has a maximum speed, a land vehicle or ship should always be close to the Earth's surface, and every aircraft has a maximum altitude above which it cannot fly.

Where a Kalman filter is used to align and calibrate the INS, integrate it with other sensors, as described in Section VI, or both, it may also be used for fault detection. The accelerometer and gyro biases are normally estimated as states. Therefore, if a bias estimate is several times the standard deviation specified by the manufacturer, there is likely to be a fault with the sensor. Outlying state estimates can also arise because of a lack of measurements or observability problems. However, in these cases, the state uncertainties will also be large.

The Kalman filter measurement innovations, $\delta\mathbf{z}_k^-$, provide an indication of whether the measurements and state estimates are consistent with each other. Therefore, by comparing the current innovations with their expected uncertainties and computing statistics over several epochs, errors in both the INS and the aiding sensors may be detected [3].

Where a standard IMU with three accelerometers and three gyros is used, the whole inertial navigation solution must normally be discarded if a fault is found in one of the sensors. However, if additional sensors are included, a navigation solution may be maintained. These systems are known as redundant IMUs [58, 59]. The sensors are normally mounted in a skewed configuration so that all six degrees of freedom can be observed using any three accelerometers and any three gyros. Where external information is available for fault detection, recovery from faults is achievable using four accelerometers and four gyros.

The outputs of four skewed accelerometers or gyros may be compared with one another to determine whether they are in agreement. This is known as consistency checking [3] and can detect a fault without external information. However, it can-

not identify the faulty sensor. This requires five accelerometers and gyros, enabling different combinations of four sensors to be tested for consistency. If a fault is detected immediately, the inertial navigation solution may be protected simply by excluding further measurements from the faulty sensor. However, to protect against slow-onset faults, parallel inertial navigation solutions computed from different sensor combinations must be maintained.

X. CONCLUDING REMARKS

Inertial sensors have been used in navigation for many decades. However, the field is still evolving. The development of small, light, low-cost sensors has greatly expanded the number of applications. At the same time, advances such as GNSS integration, step detection, and context-specific motion constraints have enabled better navigation performance to be extracted from lower quality sensors. Looking to the future, developments in accelerometer and gyro technology are likely to offer higher performance at lower cost. At the same time, new navigation and positioning techniques are being developed for use alongside inertial sensors in integrated systems [60].

Further details on all of the topics covered in this tutorial may be found in [3] and the references therein, some of which are listed in the References section. ◆

REFERENCES

- [1] Weiner, T. F. Theoretical analysis of gimbaless inertial reference equipment using delta-modulated instruments. Sc.D. thesis, Massachusetts Institute of Technology, Cambridge, 1962.
- [2] Savage, P. G. Blazing gyros: The evolution of strapdown inertial navigation technology for aircraft. *Journal of Guidance, Control, and Dynamics*, **35** (May–June 2013), 637–655.
- [3] Groves, P. D. *Principles of GNSS, Inertial, and Multisensor Integrated Navigation Systems* (2nd ed.). Boston, MA: Artech House, 2013.
- [4] Titterton, D. H., and Weston, J. L. *Strapdown Inertial Navigation Technology* (2nd ed.). Stevenage, United Kingdom: IEE, 2004.
- [5] Lawrence, A. *Modern Inertial Technology* (2nd ed.). New York: Springer-Verlag, 2001.
- [6] Kempe, V. *Inertial MEMS Principles and Practices*. Cambridge, United Kingdom: Cambridge University Press, 2011.
- [7] Karnick, D., et al. Honeywell gun-hard inertial measurement unit (IMU) development. In *Proceedings of the Institute of Navigation National Technical Meeting*, San Diego, CA, Jan. 2007, 718–724.
- [8] McGuinness, H. J., Rakholia, A. K., and Biedermann, G. W. High data-rate atom interferometer for measuring acceleration. *Applied Physics Letters*, **100** (2012), Article ID 011106.
- [9] Brown, D., et al. Atom interferometric gravity sensor system. In *Proceedings of the IEEE/ION Position Location and Navigation Symposium (PLANS)*, Myrtle Beach, SC, Apr. 2012, 30–37.
- [10] Grewal, M. S., Weill, L. R., and Andrews, A. P. *Global Positioning Systems, Inertial Navigation, and Integration* (2nd ed.). New York: Wiley, 2007.
- [11] Donley, E. A. Nuclear magnetic resonance gyroscopes. In *Proceedings of the IEEE Sensors 2010*, Waikoloa, HI, Nov. 2010, 17–22.

- [12] Stockton, J. K., Takase, K., and Kasevich, M. A. Absolute geodetic rotation measurement using atom interferometry. *Physical Review Letters*, **107** (2011), Article ID 133001.
- [13] Edwan, E., Knedlik, S., and Loffeld, O. Constrained angular motion estimation in a gyro-free IMU. *IEEE Transactions on Aerospace and Electronic Systems*, **47** (Jan. 2011), 596–610.
- [14] El-Sheimy, N. The potential of partial IMUs for land vehicle navigation. *Inside GNSS* (Spring 2008), 16–25.
- [15] Pethel, S. J. Test and evaluation of high performance micro electro-mechanical system based inertial measurement units. In *Proceedings of the IEEE/ION Position Location and Navigation Symposium (PLANS)*, San Diego, CA, Apr. 2006, 772–794.
- [16] Yuksel, Y., El-Sheimy, N., and Noureldin, A. Error modeling and characterization of environmental effects for low cost inertial MEMS units. In *Proceedings of the IEEE/ION Position Location and Navigation Symposium (PLANS)*, Palm Springs, CA, May 2010, 598–612.
- [17] Jekeli, C. *Inertial Navigation Systems with Geodetic Applications*. Berlin, Germany: de Gruyter, 2000.
- [18] Savage, P. G. *Strapdown Analytics: Parts 1 and 2*. Maple Plain, MN: Strapdown Associates, 2000.
- [19] Farrell, J. A. *Aided Navigation*. New York: McGraw-Hill, 2008.
- [20] Britting, K. R. *Inertial Navigation Systems Analysis*. New York: Wiley, 1971. (Republished by Norwood, MA: Artech House, 2010.)
- [21] National Imagery and Mapping Agency (now NGA). Department of defense world geodetic system 1984, Tech Rep. TR8350.2, 3rd ed., 1997.
- [22] Iliffe, J., and Lott, R. *Datums and Map Projections for Remote Sensing, GIS and Surveying* (2nd ed.). Edinburgh, United Kingdom: Whittles Publishing, 2008.
- [23] Savage, P. G. Strapdown inertial navigation integration algorithm design. Part 1: Attitude algorithms. *Journal of Guidance Control and Dynamics*, **21** (Jan.–Feb. 1998), 19–28; Erratum: **22** (Mar.–Apr. 1999), 384. Strapdown inertial navigation integration algorithm design. Part 2: Velocity and position algorithms. *Journal of Guidance Control and Dynamics*, **21** (Mar.–Apr. 1998), 208–221; Erratum: **27** (Mar.–Apr. 2004), 318.
- [24] Levinson, E., and Majure, R. Accuracy enhancement techniques applied to the marine ring laser inertial navigator (MARLIN). *Navigation*, **34** (Spring 1987), 64–86.
- [25] Hua, C. Gyrocompass alignment with base motions: Result for a 1 nm/h INS/GPS system. *Navigation*, **47** (Summer 2000), 65–74.
- [26] Langley, R. B. Getting your bearings: The magnetic compass and GPS. *GPS World* (Sept. 2003), 70–81.
- [27] Zhao, Y. *Vehicle Location and Navigation Systems*. Norwood, MA: Artech House, 1997.
- [28] Mather, C. J., Groves, P. D., and Carter, M. R. A man motion navigation system using high sensitivity GPS, MEMS IMU and auxiliary sensors. In *Proceedings of the Institute of Navigation GNSS 2006*, Fort Worth, TX, Sept. 2006, 2704–2714.
- [29] Afzal, M. H. Use of Earth's magnetic field for pedestrian navigation, Ph.D. dissertation, University of Calgary, Canada, July 2011.
- [30] Gebre-Egziabher, D., et al. Calibration of strapdown magnetometers in magnetic field domain. *Journal of Aerospace Engineering*, **19**, 2 (2006), 87–102.
- [31] Guo, P., et al. The soft iron and hard iron calibration method using extended Kalman filter for attitude and heading reference system. In *Proceedings of the IEEE/ION Position Location and Navigation Symposium (PLANS)*, Monterey, CA, May 2008, 1167–1174.
- [32] Kayton, M., and Wing, W. G. Attitude and heading references. In *Avionics Navigation Systems* (2nd ed.). New York: Wiley, 1997, pp. 426–448.
- [33] Kaplan, E. D., and Hegarty, C. J. *Understanding GPS Principles and Applications* (2nd ed.). Norwood, MA: Artech House, 2006.
- [34] Misra, P., and Enge, P. *Global Positioning System Signals, Measurements, and Performance* (2nd ed.). Lincoln, MA: Ganga-Jamuna Press, 2006.
- [35] Gelb, A. *Applied Optimal Estimation*. Cambridge, MA: MIT Press, 1974.
- [36] Brown, R. G., and Hwang, P. Y. C. *Introduction to Random Signals and Applied Kalman Filtering* (3rd ed.). New York: Wiley, 1997.
- [37] Grewal, M. S., and Andrews, A. P. *Kalman Filtering: Theory and Practice* (2nd ed.). New York: Wiley, 2000.
- [38] Simon, D. *Optimal State Estimation*. New York: Wiley, 2006.
- [39] Grejner-Brzezinska, D. A., Yi, Y., and Toth, C. K. Bridging gaps in urban canyons: The benefits of ZUPTs. *Navigation*, **48** (Winter 2001), 217–225.
- [40] Foxlin, E. Pedestrian tracking with shoe-mounted inertial sensors. *IEEE Computer Graphics and Applications* (Nov.–Dec. 2005), 38–46.
- [41] Godha, S., Lachapelle, G., and Cannon, M. E. Integrated GPS/INS system for pedestrian navigation in a signal degraded environment. In *Proceedings of the Institute of Navigation GNSS 2006*, Fort Worth, TX, Sept. 2006, 2151–2164.
- [42] Groves, P. D., et al. Inertial navigation versus pedestrian dead reckoning: Optimizing the integration. In *Proceedings of the Institute of Navigation GNSS 2007*, Fort Worth, TX, Sept. 2007, 2043–2055.
- [43] Aggarwal, P., et al., *MEMS-Based Integrated Navigation*. Norwood, MA: Artech House, 2010.
- [44] Dissanayake, G., et al. The aiding of a low-cost strapdown inertial measurement unit using vehicle model constraints for land vehicle applications. *IEEE Transactions on Robotics and Automation*, **17** (Oct. 2001), 731–747.
- [45] Niu, X., Nassar, S., and El-Sheimy, N. An accurate land-vehicle MEMS IMU/GPS navigation system using 3D auxiliary velocity updates. *Navigation*, **54** (Fall 2007), 177–188.
- [46] Wu, Y., Goodall, C., and El-Sheimy, N. Self-calibration for IMU/odometer land navigation: simulation and test results. In *Proceedings of the Institute of Navigation International Technical Meeting*, San Diego, CA, Jan. 2010, 839–849.
- [47] Vinande, E., Axelrad, P., and Akos, D. Mounting-angle estimation for personal navigation devices. *IEEE Transactions on Vehicular Technology*, **59** (Mar. 2010), 1129–1138.
- [48] Ryan, J., and Bevly, D. Robust ground vehicle constraints for aiding stand alone INS and determining inertial sensor errors. In *Proceedings of the Institute of Navigation International Technical Meeting*, Newport Beach, CA, Jan. 2012, 374–384.
- [49] Borenstein, J., Ojeda, L., and Kwanmuang, S. Heuristic reduction of gyro drift for personnel tracking systems. *Journal of Navigation*, **62** (Jan. 2009), 41–58.
- [50] Abdulrahim, K., et al. Using constraints for shoe mounted indoor pedestrian navigation. *Journal of Navigation*, **65** (Jan. 2012), 15–28.
- [51] Judd, T. A personal dead reckoning module. In *Proceedings of the Institute of Navigation GPS 1997*, Kansas, MO, Sept. 1997, 47–51.

- [52] Käppi, J., Syrjärinne, J., and Saarinen, J. MEMS-IMU based pedestrian navigator for handheld devices. In *Proceedings of the Institute of Navigation GPS 2001*, Salt Lake City, UT, Sept. 2001, 1369–1373.
- [53] Collin, J., Mezentsev, O., and Lachapelle, G. Indoor positioning system using accelerometry and high accuracy heading sensors. In *Proceedings of the Institute of Navigation GPS/GNSS 2003*, Portland, OR, Sept. 2003, 1164–1170.
- [54] Ladetto, Q. On foot navigation: Continuous step calibration using both complementary recursive prediction and adaptive Kalman filtering. In *Proceedings of the Institute of Navigation GPS 2000*, Salt Lake City, UT, Sept. 2000, 1735–1740.
- [55] Leppäkoski, H., et al. Error analysis of step length estimation in pedestrian dead reckoning. In *Proceedings of the Institute of Navigation GPS 2002*, Portland, OR, Sept. 2002, 1136–1142.
- [56] Park, C. G., et al. Adaptive step length estimation with awareness of sensor equipped location for PNS. In *Proceedings of the Institute of Navigation GNSS 2007*, Fort Worth, TX, Sept. 2007, 1845–1850.
- [57] Pei, L., et al. Using motion-awareness for the 3D indoor personal navigation on a smartphone. In *Proceedings of the Institute of Navigation GNSS 2011*, Portland, OR, Sept. 2011, 2906–2913.
- [58] Gilmore, J. P., and Cooper, R. J. SIRU development: Final Report. Vol. 1: System Development. Charles Stark Draper Laboratory, Cambridge, MA, 1973.
- [59] Sukkarieh, S., et al. A low-cost redundant inertial measurement unit for unmanned air vehicles. *International Journal of Robotics Research*, **19** (Nov. 2000), 1089–1103.
- [60] Groves, P. D. The PNT boom: Future trends in integrated navigation. *Inside GNSS* (Mar.–Apr. 2013), 44–49.

BIO

Paul Groves has been researching navigation systems for 18 years. Since 2009, he has been a lecturer (academic faculty member) at University College London. Previously, he worked as a research scientist at the Defence Evaluation and Research Agency and then QinetiQ. He is interested in all aspects of navigation and leads research into navigation using raw inertial sensors, pedestrian motion modeling, advanced integration architectures, navigation using novel environmental features, and GNSS shadow matching.



He is an author of more than 70 technical publications, including the book *Principles of GNSS, Inertial and Multi-Sensor Integrated Navigation Systems*, now in its second edition. He is a fellow of the Royal Institute of Navigation and holds a bachelor's degree and doctorate in physics from the University of Oxford.